Influence of crystallographic orientation on the void growth at the grain boundaries in bi-crystals

Manjunath Dakshinamurthy[a], Katarzyna Kowalczyk-Gajewska[b], Guadalupe Vadillo[a,*]

[a] *Department of Continuum Mechanics and Structural Analysis, University Carlos III of Madrid, Avda. de la Universidad, 30, Leganés, Madrid 28911, Spain*

[b] *Institute of Fundamental Technological Research, Polish Academy of Sciences, Pawińskiego 5b, 02 106 Warsaw, Poland*

Abstract

Void growth and morphology evolution in fcc bi-crystals are investigated using crystal plasticity finite element method. For that purpose, representative volume element of bi-crystals with a void at the grain boundary are considered in the analysis. Grain boundary is assumed initially perpendicular/coaxial with the straight sides of the cell. Fully periodic boundary conditions are prescribed in the representative volume element and macroscopic stress triaxiality and Lode parameter are kept constant during the whole deformation process. Three different pairs of crystal orientations characterized as hard-hard, soft-soft and soft-hard has been employed for modelling the mechanical response of the bi-crystal. Simulations are performed to study the implications of triaxiality, Lode parameter and crystallographic orientation on slip mechanism, hardening and hence void evolution. The impact of void presence and its growth on the heterogeneity of lattice rotation and resulting grain fragmentation in neighbouring areas is also analysed and discussed.

Keywords:
Crystal plasticity; Bi-crystals; Void growth; Stress Triaxiality; Lode parameter; Unit cell calculations.

1. Introduction

One of the common challenges to overcome when using advanced metals and alloys in engineering applications is their insufficient ductility (Fourmeau et al., 2013; Basu et al., 2017). Strengthening of materials is usually achieved by introduction of precipitates, second phase particles or new grain boundaries while at the same time these additions are possible sites of damage/fracture initiation, cf. (Yerra et al., 2010). Predominant mechanisms of ductile failure in polycrystaline metals are nucleation, growth and coalescence of micro-voids (small scale voids), cf. (Benzerga and Besson, 2001). Accounting for these mechanisms in modelling, a family of macroscopic approximations were proposed, namely prominent models like Gurson-types models (Gurson, 1977; Tvergaard and Needleman, 1984), their extension in later works by taking into

*Corresponding author.
Email addresses: mdakshin@ing.uc3m.es (Manjunath Dakshinamurthy), kkowalcz@ippt.pan.pl (Katarzyna Kowalczyk-Gajewska), gvadillo@ing.uc3m.es (Guadalupe Vadillo)

account many aspects such as void shape, size, volume fraction and distribution of voids, as well as distinct features of the constitutive model of a virgin material such as strain and kinematic hardening, viscoplasticity and plastic anisotropy. For respective contributions see extensive review by Besson (2010). Such type of approach was also used to formulate the micro-scale Gurson-type yield condition for single crystal (Han et al., 2013; Paux et al., 2015). In the case of Han et al. (2013) such condition is the result of micromechanical analysis based on variational estimates due to de Botton and Ponte Castañeda (1995). Note that, there are number of papers in which such variational approach is directly applied to estimate the yield surface of single crystal with voids (Mbiakop et al., 2015; Song and Castañeda, 2017).

On the micro-scale, two failure modes have been found to be operational in parallel: cleavage and dimple fracture (Papaefthymiou et al., 2006). Studies of Kadkhodapour et al. (2011a,b); Lani et al. (2007); Furnémont et al. (2007) have reported different types of damage mechanisms based on their experimental work with the help of SEM and light optical microscopy. By experimental observations, nucleation of voids is related to the fracture and decohesion of second phase particles or other precipitates. The next steps in understanding the failure process are intergranular fracture along high angle boundary (HAB) and microvoid-induced transgranular fracture. For example, such observations have been made for aluminium alloys AA7XXX subjected to the solution treatment along the processing route, which resulted in partial recrystallization (Dorward and Beerntsen, 1995; Deshpande et al., 1998). For such alloys it was observed that precipitates are often grouped along HABs which promotes intergranular fracture along them. Importance of HAB as a possible location of void growth has been also confirmed by molecular dynamics simulations (Bringa et al., 2010). Additionally, as seen in Morere et al. (2000), concentration of precipitates is also observed along subgrain boundaries, characterized by a low misorientation angle, together with associated intersubgranular failure. It is also worth to note that the effect of crystal orientation and the grain boundary was observed under shock loading conditions for copper bi-crystal by Perez-Bergquist et al. (2011). They observed formation of voids both at the grain boundary and within each crystal, with the number and shape of voids highly dependent on the crystallographic orientation. Although this type of loading is beyond the scope of this paper, these experiments confirm the role of crystal anisotropy and grain boundaries in the failure of crystalline material.

Although there is quite a lot numerical studies of single crystals with voids, (O'Regan et al., 1997; Potirniche et al., 2006; Yerra et al., 2010; Srivastava and Needleman, 2015a; Selvarajou et al., 2019) very few numerical studies have been dedicated to the studies on void in bi-crystals. One can mention earlier works by Liu et al. (2009) in which the fcc bi-crystal under uniaxial tension was investigated to assess the effect of boundary inclination and the crystallographic orientation and misorientation on the void growth and the plastic deformation distribution around the voids. Liu et al. (2007, 2010) studied mechanisms of coalescence of voids located at adjacent grains in bi-crystal unit cell using finite element calculations. Recently, Jeong et al. (2018) considered the unit cells with a void inside a grain, at a grain boundary and at a triple junction. The effect of crystal orientation on the flow strength and growth rate of the void was discussed under prescribed boundary conditions for constant stress triaxialities. Even though studies mentioned above shed light on the behaviour of void at boundary on bi-crystals, there are still open questions, like the effect of neighbouring grain orientation on void shape, the effect of stress state on void growth or void collapse behaviour among others.

Appreciating the important role of a grain boundary on void behaviour, as noted by Deshpande et al. (1998); Bringa et al. (2010); Morere et al. (2000), the main purpose of the current work is to study the factors affecting void growth and morphology evolution in bi-crystals, such as stress triaxiality and Lode parameter and the relative orientation between grains, focusing specifically on voids originating in high angle grain boundaries. The response of bi-crystals containing a void at the grain boundary are also compared with the response of a single crystal with a void.

The paper is constructed as follows, after this introductory section, the problem formulation including crystal plasticity framework, representative volume element and prescribed boundary conditions are presented in Section 2. In Section 3 results of FE simulations are compared from single crystals with bi-crystals and from different bi-crystals RVEs. The paper is closed by conclusions. Details of implementation of user defined multi-point constraints (MPC) subroutine for controlling stress state (stress triaxiality and Lode parameter) and periodic boundary conditions (PBC) are included in the Appendix.

Table 1: Slip systems $\{\widetilde{\mathbf{m}}^\alpha, \widetilde{\mathbf{n}}^\alpha\}$ of the FCC crystal structure

α	$\widetilde{\mathbf{n}}_\alpha$	$\widetilde{\mathbf{m}}_\alpha$	α	$\widetilde{\mathbf{n}}_\alpha$	$\widetilde{\mathbf{m}}_\alpha$
1	(111)	$[\bar{1}01]$	7	$(\bar{1}11)$	$[0\bar{1}1]$
2	(111)	$[0\bar{1}1]$	8	$(\bar{1}11)$	$[101]$
3	(111)	$(1\bar{1}0]$	9	$(\bar{1}11)$	$[110]$
4	$(1\bar{1}1)$	$[\bar{1}01]$	10	$(11\bar{1})$	$[\bar{1}10]$
5	$(1\bar{1}1)$	$[011]$	11	$(11\bar{1})$	$[101]$
6	$(1\bar{1}1)$	$[110]$	12	$(11\bar{1})$	$[011]$

2. Problem formulation

Three dimensional finite element calculations are carried out to model the response of voids, located at the grain boundary of a bi-crystal, under triaxial loading conditions using a unit cell model. The unit cell is modelled as an fcc single crystal with the 12 potentially active slip systems taken to be $\{111\}\langle 110\rangle$ (Table 1). Finite element analyses are carried out using a rate dependent crystal plasticity constitutive relation in the large deformation framework. Description of the crystal plasticity model and material parameters used for calculations are given below. The plastic parameters of the material analyzed in this work correspond to annealed OFHC copper (Kalidindi et al., 1992).

2.1. Constitutive model for a single crystal

Description of kinematics follows the standard large strain deformation framework. The multiplicative decomposition is applied, according to which the deformation gradient $\mathbf{F}$ is the product of an elastic part $\mathbf{F}^{\mathrm{e}}$ and a plastic part $\mathbf{F}^{\mathrm{p}}$, namely:

$$\mathbf{F} = \mathbf{F}^{\mathrm{e}}\mathbf{F}^{\mathrm{p}}. \tag{1}$$

Table 2: Material parameters for crystal plasticity model (Han et al., 2013; Kalidindi et al., 1992)

Parameter	**Notation**	**Value**
Reference shear rate	$\dot{\gamma}_0$ (s^{-1})	0.001
Inverse of strain rate sensitivity	p_1	20
Initial critical resolved shear stress	$\hat{\tau}_0$ (MPa)	20
Initial strain hardening modulus	h_0 (MPa)	180
Saturated critical resolved shear stress	$\hat{\tau}_s$ (MPa)	117
Strain hardening exponent	p_2	2.25
Self-hardening coefficient	$q_{\alpha\beta}$ ($\alpha = \beta$)	1
Latent hardening coefficient	$q_{\alpha\beta}$ ($\alpha \neq \beta$)	1.4
Elastic constants		
	c_{11} (GPa)	199
	c_{12} (GPa)	136
	c_{44} (GPa)	105

It is assumed that the plastic deformation occurs by dislocation glide on slip systems, therefore the evolution of the plastic part follows the equation

$$\dot{\mathbf{F}}^{\mathrm{p}} = \left(\sum_{\alpha=1}^{N^{\mathrm{S}}} \dot{\gamma}_\alpha \widetilde{\mathbf{M}}_\alpha \right) \mathbf{F}^{\mathrm{p}} , \quad \widetilde{\mathbf{M}}_\alpha = \widetilde{\mathbf{m}}_\alpha \otimes \widetilde{\mathbf{n}}_\alpha \tag{2}$$

$\widetilde{\mathbf{M}}_\alpha$ being a Schmid tensor where the slip directions $\widetilde{\mathbf{m}}_\alpha$ and planes $\widetilde{\mathbf{n}}_\alpha$ are specified in the intermediate configuration. It should be noted that the plastic deformation described by Eq.2 is volume preserving, $\det \mathbf{F}^{\mathrm{p}} = 1$, since $\widetilde{\mathbf{m}}_\alpha \cdot \widetilde{\mathbf{n}}_\alpha = 0$. The current orientation of crystallographic directions and planes can be found using the elastic part of the deformation gradient as follows

$$\mathbf{n}(t)_\alpha = (\mathbf{F}^{\mathrm{e}T})^{-1} \widetilde{\mathbf{n}}_\alpha , \quad \mathbf{m}(t)_\alpha = \mathbf{F}^{\mathrm{e}} \widetilde{\mathbf{m}}_\alpha . \tag{3}$$

Because the face centred cubic (fcc) crystal structure is considered in the study, the dislocations glide happens on the $\{111\}$ planes in $\langle 110 \rangle$ directions. For the $N^{\mathrm{S}} = 12$ slip systems, the slip planes and directions are listed in Table 1.

The shear rate $\dot{\gamma}_\alpha$ on a given slip system α is related the stress state by the phenomenological visco-plastic type power law (Asaro and Needleman, 1985)

$$\dot{\gamma}_\alpha = \dot{\gamma}_0 \left| \frac{\tau_\alpha}{\hat{\tau}_\alpha} \right|^{p_1} \operatorname{sign}(\tau_\alpha). \tag{4}$$

with the resolved shear stress

$$\tau_\alpha = \widetilde{\mathbf{T}} \cdot \widetilde{\mathbf{M}}_\alpha \tag{5}$$

where the parameter $\dot{\gamma}_0$ is the reference shear rate, p_1 is the inverse of the strain rate sensitivity parameter and $\widetilde{\mathbf{T}}$ is the Mandel stress. When the elastic strains are small as compared to the

inelastic ones, the Mandel stress can be approximated by the IInd Piola-Kirchhoff stress pushed forward to the intermediate configuration $\widetilde{\mathbf{S}}$, namely:

$$\widetilde{\mathbf{T}} = \underbrace{\left(\mathbf{F}^{\mathrm{eT}}\mathbf{F}^{\mathrm{e}}\right)}_{\approx\mathbf{I}}\widetilde{\mathbf{S}} \approx \mathbf{F}^{\mathrm{p}}\mathbf{S}\mathbf{F}^{\mathrm{pT}} \tag{6}$$

The stress tensor $\widetilde{\mathbf{S}}$ is calculated with help of the hyperelastic law assuming the Kirchhoff-type function of free energy density per unit volume in the reference configuration

$$\widetilde{\mathbf{S}} = \frac{\partial \Psi}{\partial \mathbf{E}^{\mathrm{e}}} = \mathbb{C}\cdot\mathbf{E}^{\mathrm{e}} \quad \text{where} \quad \mathbf{E}^{\mathrm{e}} = \left[\frac{1}{2}\left(\mathbf{F}^{\mathrm{eT}}\mathbf{F}^{\mathrm{e}} - \mathbf{I}\right)\right] \tag{7}$$

with $\mathbb{C}$ the elastic IVth order stiffness tensor.

The critical resolved shear stress $\hat{\tau}_\alpha$, obeys the following evolution rule (Kalidindi et al., 1992)

$$\dot{\hat{\tau}}_\alpha = h_0 \sum_{\beta=1}^{N^{\mathrm{S}}} q_{\alpha\beta}\left(1 - \frac{\hat{\tau}_\beta}{\hat{\tau}_{\mathrm{s}}}\right)^{p_2} |\dot{\gamma}_\beta| \tag{8}$$

where h_0 is the initial hardening rate, $\hat{\tau}_{\mathrm{s}}$ the saturation resistance, p_2 the hardening exponent and $q_{\alpha\beta}$ the cross hardening coefficient matrix. The model parameters for elasticity and plasticity are given in Table 2.

The constitutive equations mentioned above are implemented into a user subroutine UMAT in ABAQUS/Standard (2019). The implementation of the crystal plasticity model follows the fully implicit time integration procedure with the consistent material tangent operator presented by Meissonnier et al. (2001).

2.2. Representative Volume Element and boundary conditions

In this section, representative unit cells used for studying the behaviour of a void in both single crystal and bi-crystal cases are described briefly. For studying the void response in a single crystal, the representative volume element consisting of a cubic cell with a initial spherical void at the center as shown in figure 1 is considered and initial void volume fraction $f_0 = 0.0044$ is used. The initial void volume fraction is selected to be small, so that we can study the void shape changes and its evolutions at large deformations. Void volume fraction is calculated as $f_0 = V_{void}/V_{cell}$, where V_{cell} is the initial volume of the cell and V_{void} is the initial volume of the void. The complete matrix-void zone is discretized into 90000 C3D8R elements. For the bi-crystal case, representative unit cell consists in a cube with a void inside divided into two equal parts, each half having half spherical void with $f_0 = 0.0022$, as shown in figure 4. Finite element mesh and number of elements in the mesh are the same as for the single crystal case. Depending on the cases to be studied, different crystallographic orientations are assigned to each half of the bi-crystal matrix and will be discussed in detail in the next section.

Initially, unit cells are aligned such that the edges of the unit cell are parallel to the global XYZ axes. In the case of the bi-crystal cell, interface (grain boundary) between the two halves of the unit cell is perpendicular to the global X axis. The notation adopted here denotes each orientation by the crystallographic directions, aligned with the main loading direction. The main loading direction is parallel to the X axis and the secondary loading direction is parallel to Z

or Y axis depending on the selected Lode parameter. Six crystallographic orientations are used in this study. Orientations are given in terms of the Bunge Euler angles and crystallographic planes parallel to each loading direction. Pole figures for the orientations considered are shown in figure 1. For simplicity, each 6 orientations will be henceforth called O1 - O6 as shown in Table 3.

Macroscopic Cauchy stress σ_{ij} components are related to the microscopic Cauchy stresses $\bar{\sigma}_{ij}$ through the relations:

$$\sigma_{ij} = \frac{1}{V_{cell}} \int_{V_{cell}} \bar{\sigma}_{ij} \; dV_{cell} \tag{9}$$

and the definition of macroscopic equivalent stress σ_{eqv}, triaxiality T and Lode parameter L are given by:

$$\sigma_{eqv} = \sqrt{\frac{3}{2} \; \sigma'_{ij}\sigma'_{ij}}; \quad T = \frac{\sigma_h}{\sigma_{eqv}}; \quad L = \frac{2\sigma_2 - \sigma_1 - \sigma_3}{\sigma_1 - \sigma_3} \tag{10}$$

with

$$\sigma'_{ij} = \sigma_{ij} - \sigma_h \delta_{ij}; \qquad \sigma_h = \frac{\sigma_{ii}}{3} \tag{11}$$

and σ_1, σ_2 and σ_3 the principal macroscopic true stress components. Following Srivastava and Needleman (2015a), an equivalent strain is calculated based on the following numerical volume average of local logarithmic strain $\bar{\varepsilon}_{ij}$, namely:

$$\langle \varepsilon_{ij} \rangle = \frac{1}{V_{matrix}} \int_{V_{matrix}} \bar{\varepsilon}_{ij} dV_{matrix} \tag{12}$$

where V_{matrix} denotes the volume of bi-crystal excluding the void. It must be stressed that, in general, this volume averaged value $\langle \varepsilon_{ij} \rangle$ is not equal to the macroscopic logarithmic strain as long as deformation is non-uniform. The definition of the equivalent strain is then proposed as follows:

$$\varepsilon_{eqv} = \sqrt{\frac{2}{3} \langle \varepsilon'_{ij} \rangle \langle \varepsilon'_{ij} \rangle} \quad \text{where} \quad \langle \varepsilon'_{ij} \rangle = \langle \varepsilon_{ij} \rangle - \varepsilon_h \delta_{ij} \, ; \quad \varepsilon_h = \frac{\langle \varepsilon_{ii} \rangle}{3} \tag{13}$$

This value is used only for the purpose of graphical presentation of results.

Proper boundary conditions are important for studying symmetric (O1, O2, O3) and non symmetric (O4, O5, O6) crystallographic orientations, as crystals tend to come shear strain components. If shear strain components are constrained, cells deformation behaviour is affected and hence void growth. In order to avoid this effect in our RVEs, fully periodic boundary conditions are applied to the cell in all three directions, thereby allowing crystal to deform freely without constraints. The main idea of periodic boundary conditions is that the relative displacement between opposing nodes is the same, i.e., the nodal displacement of opposite nodes is coupled, but still allowing global strain in this direction. Note that by prescribing periodic boundary conditions we are analysing a unit cell which corresponds to the configuration representing a bi-crystal laminate with voids periodically distributed along every second grain boundary. In addition, the values of T and L are prescribed throughout the numerical simulations as constant values. This is achieved by implementing a user defined multi point constraints subroutine in the framework of ABAQUS/Standard (2019). Detailed description of periodic boundary conditions and multi point constraints implementations in ABAQUS/Standard (2019) are given in Appendix A.

In this work four values of stress triaxiality ($T = 0,\ 1/3,\ 2/3,\ 1$) and three values of Lode parameter ($L = 0,\ \ 1,\ -1$) with fully periodic boundary conditions are considered. Some of the combinations of triaxiality and Lode parameters analyzed corresponds to general loading scenarios used in experiments and simple loading conditions, like $T = 1/3,\ \ L = -1$ (uniaxial tension), $T = 2/3,\ \ L = 1$ (biaxial tension) and $T = 0,\ \ L = 0$ (pure shear stress). Since anisotropic material model is assumed in each case orientation of principal stress axes is explicitly specified with respect to material anisotropy axes. It should be underlined that in the considered examples dependence of the void growth on the Lode parameter cannot be studied separately from the effect of plastic anisotropy. Finally, as our material model is rate dependent, a value of $\dot{\varepsilon}_{eqv}/\dot{\gamma}_0$ in the range $(100 - 150)$ is also assured in all the simulations performed in this work.

Table 3: Orientation of single crystal matrix for different RVEs in terms of Euler angles. The Euler angles are defined with respect to global axis (X,Y,Z)

RVE	**Bunge Euler angles (°)** (ϕ_1, Φ, ϕ_2)	**Crystallographic orientation on global coordinates X-Z**
O1	(0,0,0)	[100] -[001]
O2	(0,45,0)	[100] -[011]
O3	(45,0,0)	[110] -[001]
O4	(45,54.73,0)	$[1\bar{1}0]$ -[111]
O5	(0,45,54.73)	[111] -$[1\bar{1}0]$
O6	(45,35.26,90)	$[1\bar{1}1]$ -$[\bar{1}12]$

2.3. Single crystal without voids

Before studying the void response in single crystal and bi-crystal, we will first study the response of single crystal without void for different loading conditions (Lode parameters $L = 0, 1, -1$) and the orientations given in Table 3 . Equivalent stress-strain curves are plotted for all the Lode parameters and orientations considered (see figures 2). Definitions of equivalent stress and strains are as given by equations 10 and 13.

Note that yielding of a single crystal without void is not affected by triaxiality parameter T since resolved shear stress in Eq. 5 depends only on the deviatoric part of stress. This leads to the conclusion that, in particular, an equivalent strain-stress curve for $L = -1$ (resp. $L = 1$) and a selected orientation is the same for uniaxial tension (resp. uniaxial compression) and biaxial compression (resp. biaxial tension). Additionally, due to the form of Eq. 4 and 5, the same response in terms of equivalent stress and strain is obtained when we only change the sign of stress. In particular, the same response is found for uniaxial tension ($L = -1$ and $T = 1/3$) and uniaxial compression ($L = 1$ and $T = -1/3$) along the same crystallographic direction. However, in view of the convention assumed in our calculations for direction of primary loading, for $L = -1$ (and $T = 1/3$) we have to do with uniaxial tension along crystallographic direction parallel to X axis, while for $L = 1$ (and $T = -1/3$) with uniaxial compression along crystallographic direction parallel to Z axis. Therefore, if the orientation is not symmetric with respect to this change, like e.g. O4, O5 or O6, we may observe different responses for $L = 1$ and $L = -1$ in Fig. 2. It can be said that in this case the effect of Lode parameter is only apparent, and in fact the

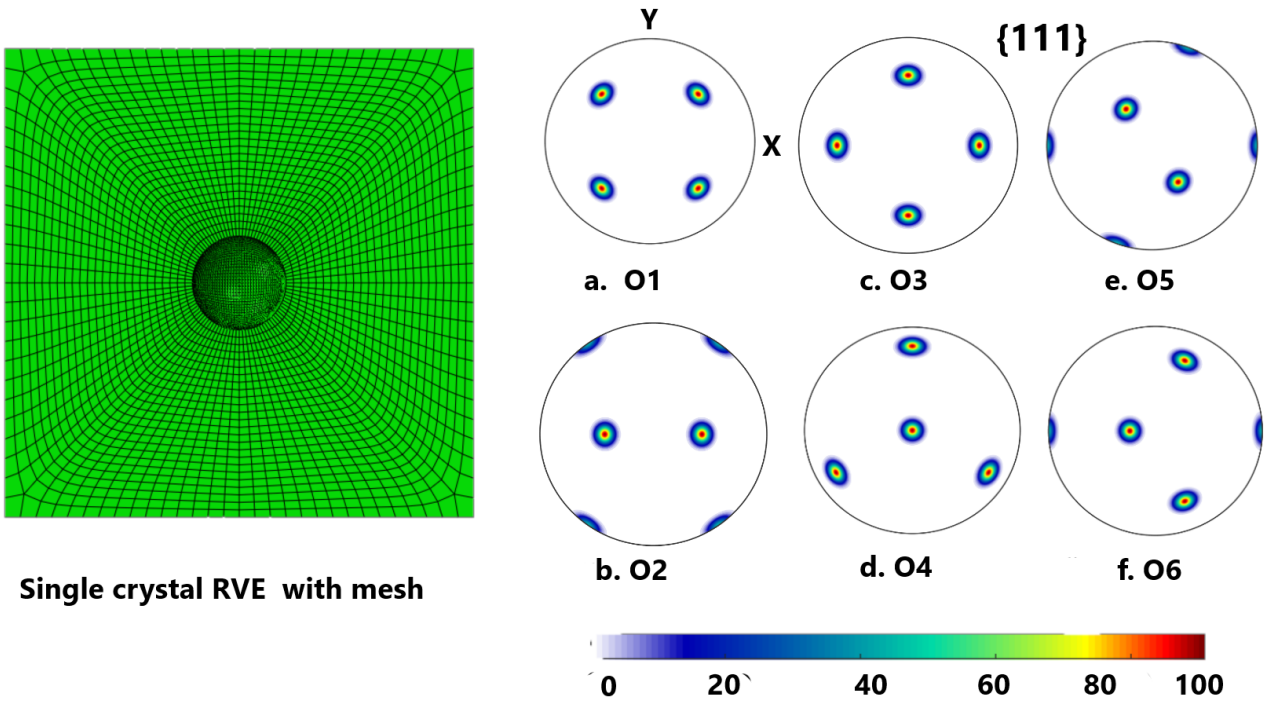

Figure 1: Cell containing a initially spherical void at its center and pole figures representing the initial orientations studied in this work.

observed difference is due to material anisotropy. Similar effects are observed when the quadratic Hill criterion is used. Such effects were thoroughly discussed by Benzerga and Besson (2001). Nevertheless in the present case also a direct effect of the Lode parameter is observed due to non-linearity of the model. The best example to demonstrate such effect is orientation O1 for which three principal directions of stress are equivalent from the point of view of crystal symmetry. In this case as expected the same stress-strain curve is found for $L = 1$ and $L = -1$, however, the response is different for $L = 0$. It is stressed that this difference is found only when $p_1 > 1$ in Eq. (4) and increases with increased non-linearity.

For Lode parameter $L = -1$, the value of equivalent stress is higher for O5 and O6 followed by O4 and least for O1, O2, O3, as shown in figure 2(a). Similarly for Lode parameter $L = 1$, the highest value of equivalent stress is for O4 followed by O5, O6 and least for O1, O2, O3 as shown in figure 2(b). Finally, as shown in figure 2(c) for $L = 0$, the highest value of equivalent stress is for O4, O5, O6 orientations and least for O1, O2, O3.

From this data, we categorized the crystal orientations into hard and soft orientations. For a given Lode parameter, the orientation with higher values of equivalent stress are considered as hard orientations and orientations with lower values of equivalent stress are considered as soft orientations. In reference to classical crystal plasticity studies, it can be said that soft (resp. hard) orientations are such which have high (resp. low) Schmid-like factor under given loading conditions.

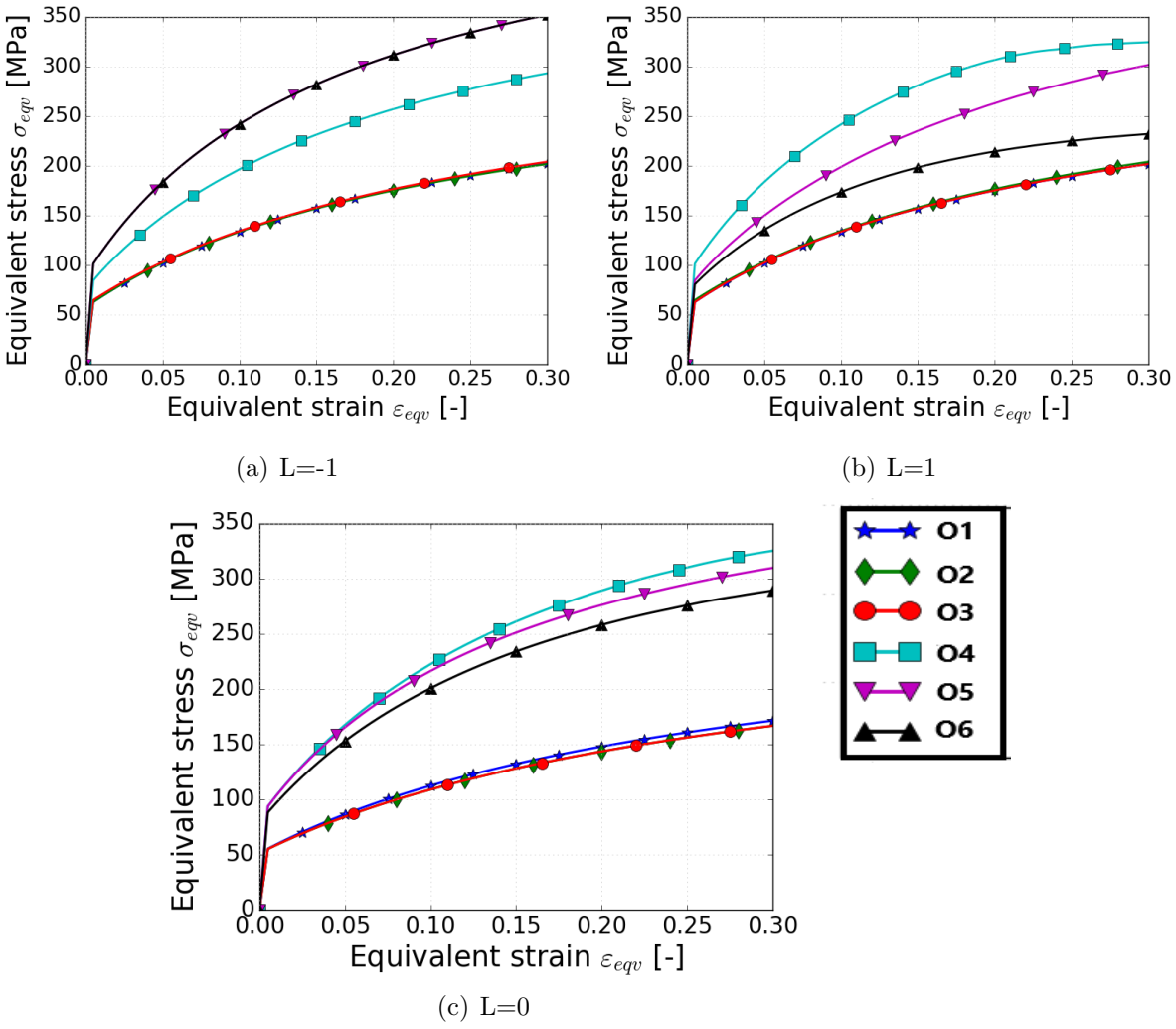

(a) L=-1

(b) L=1

(c) L=0

Figure 2: Equivalent stress - equivalent strain for single crystals without voids for different Lode parameters and different crystal orientations.The presented curves are the same for all triaxiality values considered.

3. Results and Discussion

Analytical studies on the void growth in an anisotropic rigid-plastic matrix described by the quadratic criterion performed by (Benzerga and Besson, 2001) for spherical voids, and continued by (Keralavarma and Benzerga, 2010; Keralavarma et al., 2020) for ellipsoidal voids, revealed that

this growth is governed by the formula

$$\frac{\dot{f}}{f(1-f)} \sim \frac{3}{h}\frac{1}{\tilde{\sigma}^2_{eq}(\mathbf{N})}\sinh\left(\frac{3}{h}\frac{\sigma_m}{\sigma_1}\right) \tag{14}$$

in which $\tilde{\sigma}_{eq}(\mathbf{N})$ depends on the matrix plastic anisotropy, changing with the loading directions $\mathbf{N}$ with respect to the main anisotropy axes, σ_m is the mean stress, σ_1 the yield stress in the selected direction, while h is the so-called net anisotropy invariant calculated as a single value for a given material. Accordingly an exponential void growth is affected by the triaxiality T and h, while stress direction $\mathbf{N}$ modifies mainly the proportionality coefficient through $\tilde{\sigma}^2_{eq}$. In analogy to this study Paux et al. (2015) proposed an approximate condition for the voided single crystal described by the non-quadratic regularized Schmid law, bearing mathematical similarities with the power-law rate-dependent model studied here. Authors have assessed the coefficient $\kappa \sim 1/h$ as equal to 0.506 for the fcc crystals, so it can be assumed as constant here. Therefore, qualitatively, mainly the dependencies on triaxiality and the plastic anisotropy are expected to be observed in the present analysis. Nevertheless, as it will be shown, they are additionally modified by the fact that the void is located at the bi-crystal boundary and not in the homogeneous matrix. At this moment such additional dependencies can be analyzed only numerically.

In this section results from different numerical simulations are presented. We will focus on the joint effect of stress state (T, L) and matrix crystallographic orientations (i.e. material anisotropy) on void volume fraction evolution and void morphology. We will compare results from single crystals with bi-crystals and results from different bi-crystal RVEs. In this work results of single crystal are used as reference values to compare with bi-crystals. Calculations of single crystals with voids are performed for four different crystallographic orientations O1, O2, O4, O6, 3 Lode parameters ($L = -1,\ 0,\ 1$) and 4 values of triaxialities ($T = 0,\ 1/3,\ 2/3,\ 1$). Based on the previous studies on the void growth in fcc single crystals Srivastava and Needleman (2015b), at this low and moderate triaxiality level, porosity growth is expected to be rather slow, void shape change significant and Lode parameter to have an important influence on void behavior in this respect. It should be added that for the advanced regime of the considered processes the changing shape of a void and a unit cell may additionally affect the dependencies observed in the calculations (Keralavarma and Benzerga, 2010).

3.1. Void growth in a bi-crystal

For studying the effect of grain orientation on the void growth in bi-crystals, three different representative volume elements (RVE) representing three different microstructures are created. The difference between each RVE are the crystallographic orientation assigned to the matrix of each half cell. Different orientations are assigned for half cell 1 and half cell 2, such that three different bi-crystal RVEs are formed. The orientations sets for the simulations of bi-crystals are selected from the cell calculations of single crystals without voids for different Lode parameters. By using the hard and soft orientations data, three different RVEs of bi-crystals representing; 1.soft-soft; 2. hard-hard; 3. soft-hard are created.

Orientations used for soft-soft RVE are O1 and O2 for half cell 1 and half cell 2, respectively. Similarly for hard-hard RVE, orientations used are O6 and O4 for half cell 1 and half cell 2, respectively. For soft-hard case, the orientations considered are O1 and O4 for half cell 1 and half cell 2.

It can be verified that for all three cases the grain boundary between two halves of bi-crystal is a high angle boundary. The misorientation angle and misorientation axis specified by the common crystallographic direction of two orientations is for soft-hard 56.6° and $\langle 0.590, -0.769, 0.245\rangle$, for hard-hard is 35.6° and $\langle 0.598, 0.800, 0.046\rangle$, while for soft-soft is 45° and $\langle 100\rangle$. Note that for soft-soft bi-crystal the grain boundary is a twist boundary for which its unit normal is coaxial with misorientation axis. In the remaining two cases these two vectors are inclined with respect to each other.

For bi-crystals without voids, figs. 3(a) and 3(b) represent equivalent stress- equivalent strain curves for soft-hard orientation when different Lode parameter values ($L = -1$ and $L = 1$) are prescribed in the whole cell. Green lines represent stress-strain relations for (soft) half cell 1 and red lines represent stress strain relation for (hard) half cell 2. Blue lines represent stress -strain curves when the whole bi-crystal is considered. The presented curves are the same for any triaxiality value. For comparison purposes, equivalent strain is calculated in all the cases considering the volume of the whole cell. Note that due to imposed periodic boundary condition analyzed bicrystal without a void represent the behaviour of the laminate with alternating layers with O1 (soft) and O4 (hard) crystallographic orientation. Thus the predicted stress and strain fields within each half cell are uniform, however, considerably different from each other and from the overall behaviour. For $L = 1$, fig. 3(c) presents stress-strain curves for soft-soft orientation. For $L = -1$, fig. 3(d) shows stress-strain relations for the hard-hard case. For $L = -1$ and $L = 0$, for the soft-soft bi-crystal case, stress-strain curves overlaps for both half cells and the full cell. For $L = 1$ and $L = 0$, stress-strain curves for hard-hard bi-crystal are similar as for $L = -1$. These last cases are not shown in the document for the sake of brevity.

For bi-crystals with a void, figure 4 shows FE mesh and the 3 RVEs used in the present study with their respective initial pole figures. The projection of misorientation axis is also marked in the pole figure.

The initial void volume fraction of each half cell is $f_0 = 0.0022$. Void volume fraction is calculated as $f = V_{void}/V_{cell}$, where V_{cell} is the volume of the whole cell and V_{void} is the volume of the void in the half cell. Calculating the void volume fraction for symmetric orientations O1, O2, O3 is straight forward, as the cell faces remain straight and the current volume of the cell is simply given by $(U_x + D_x) \cdot (U_y + D_y) \cdot (U_z + D_z)$, where D_x, D_y, D_z are the initial lengths of the cell in X,Y,Z direction respectively and U_x, U_y, U_z are the displacement applied at each direction. For non symmetric orientations, the initially straight sides of the unit cell along which fully periodic conditions are applied becomes curved. Since the cell faces are not straight it is not direct to calculate the current volumes of the half cells and the void. To face this problem, the following approach has been adopted in this work: The 3D (X,Y,Z) coordinates of all the nodes on the surface of the void (initially spherical) is extracted from the finite element calculations for all the time steps. By using these coordinates, void volume fraction of each half cell is calculated at each time increment with the help of convex hull algorithms (convex hull of a given set of points is the smallest convex polygon that contains all the points).

3.1.1. Void growth in a soft-soft bi-crystal.

First we will present some results related to soft-soft bi-crystal RVE. This RVE has O1 orientation for half cell 1 and O2 orientation for half cell 2. Evolution of void volume fraction f with respect to the equivalent strain ε_{eqv} for Lode parameter $L = -1$ is shown in figure 5(a) for

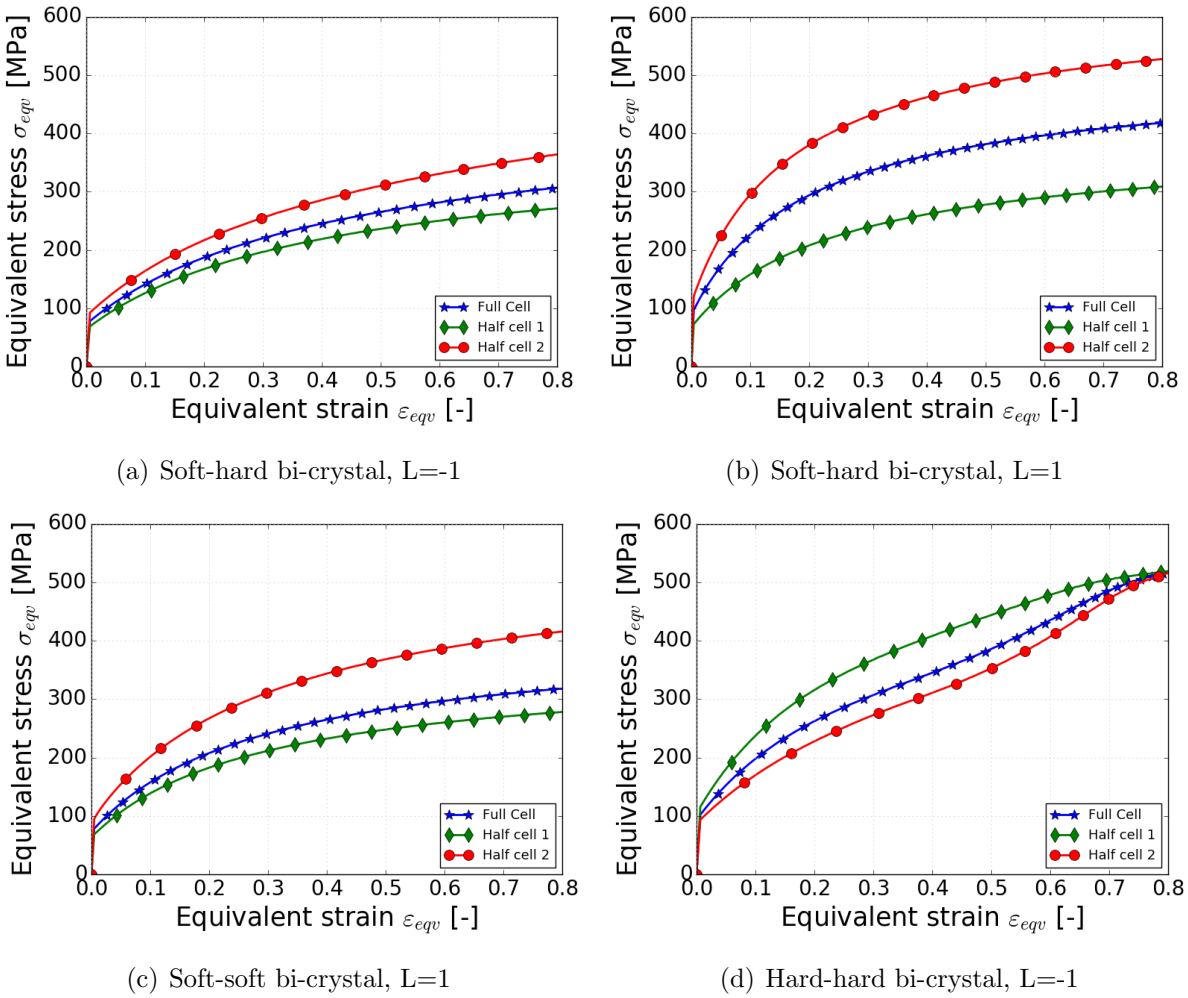

(a) Soft-hard bi-crystal, L=-1

(b) Soft-hard bi-crystal, L=1

(c) Soft-soft bi-crystal, L=1

(d) Hard-hard bi-crystal, L=-1

Figure 3: Equivalent stress - equivalent strain in half cell 1, half cell 2 and the whole bi-crystal without void for soft-hard, soft-soft and hard-hard orientation for different Lode parameters. The presented curves are the same when any value of triaxiality is prescribed in the whole cell.

different triaxialities (T). Continuous lines represent void volume fraction evolution in half cell 1 and dotted lines in half cell 2 and different colours represents different triaxiality values. For triaxility $T = 1$, $T = 2/3$ and $T = 1/3$, we can see that void volume fraction f increases with ε_{eqv} in both half cell 1 and half cell 2, whereas for triaxiality $T = 0$, void volume fraction decreases below f_0 in both half cell 1 and half cell 2. This behaviour of void volume decreasing below f_0 was also observed for porous single crystal by Srivastava and Needleman (2015a). In the case of low triaxialities, simulations are terminated when the outer surface of the voids comes in contact with each other. In general void grows faster at moderate triaxialities ($T = 1, 2/3$) compared to low triaxialities ($T = 1/3, 0$), this trend has been previously observed by Srivastava and Needleman (2015a); Yerra et al. (2010); Srivastava and Needleman (2013) for porous single crystals. Comparing void volume fraction evolution between the two half cells, we observe that difference in void volume evolution between two half cells is hardly noticeable. This results from the fact that for this case direction X of major stress $\sigma_1 \neq \sigma_2 = \sigma_3$ coincides with the same crystallographic

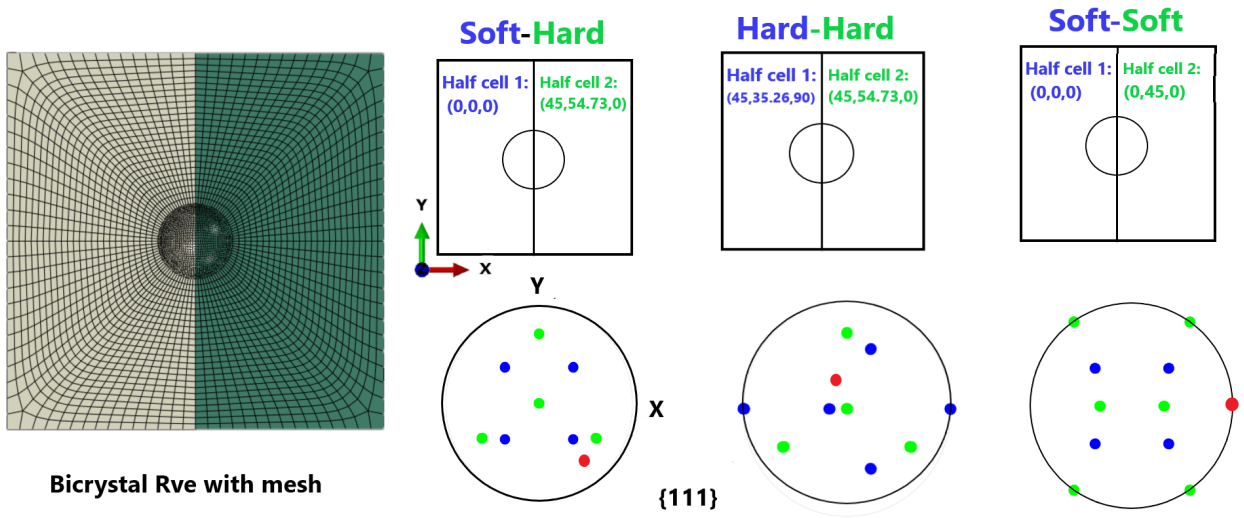

Figure 4: Different bi-crystal RVEs and respective pole figures representing the orientations used for studying the effect of matrix orientation on the void behaviour. Blue colour represents orientations in half cell 1, green colour represents orientation in half cell 2 and red colour represents the projection of misorientation axis

.

direction [001] in both half cells.

As seen from figure 5(b), for Lode parameter $L = 1$, void grows slower than for $L = -1$ (note that the vertical axis of both figures has different scale). We can see differences in void growth behaviour of half cell 1 and half cell 2 for all triaxialities considered. In this case direction Z of a minor stress $\sigma_3 \neq \sigma_1 = \sigma_2$ varies between both half cells (see Table 1). As seen in Fig. 3(c) the stress response in two half cells is then different, so the level of equivalent stress in half cell 1 is lower than in half cell 2. Following relation (14), void grows faster in half cell 1 (continuous lines) compared with void growth in half cell 2 (dotted lines) at moderate triaxialities ($T = 1, 2/3$). However, at low triaxialities ($T = 0, 1/3$) void volume in half cell 1 decreases faster as compared to void in half cell 2. To find a source of such behviour the local triaxialities have been calculated for the Cauchy stress averaged over each half cell separately. It has been found that the local triaxility in half cell 1 for case T=0 is negative and equal to -0.2, while for half cell 2 it is higher and equal to 0.23. Similarly, respective values for the case T=1/3 are 0.22 and 0.44, correspondingly. For the remaining cases local triaxialities per half cell are approximately equal to the macroscopic ones. All the values are collected in the table B.6

For Lode parameter $L = 0$, the behaviour of the void in both half cell 1 and half cell 2 are similar to the case of Lode parameter $L = 1$, hence plot of $f - \varepsilon_{eqv}$ is not presented. Among the Lode parameters considered, void growth rate is in general higher for Lode parameter $L = -1$, followed by $L = 0$ and $L = 1$.

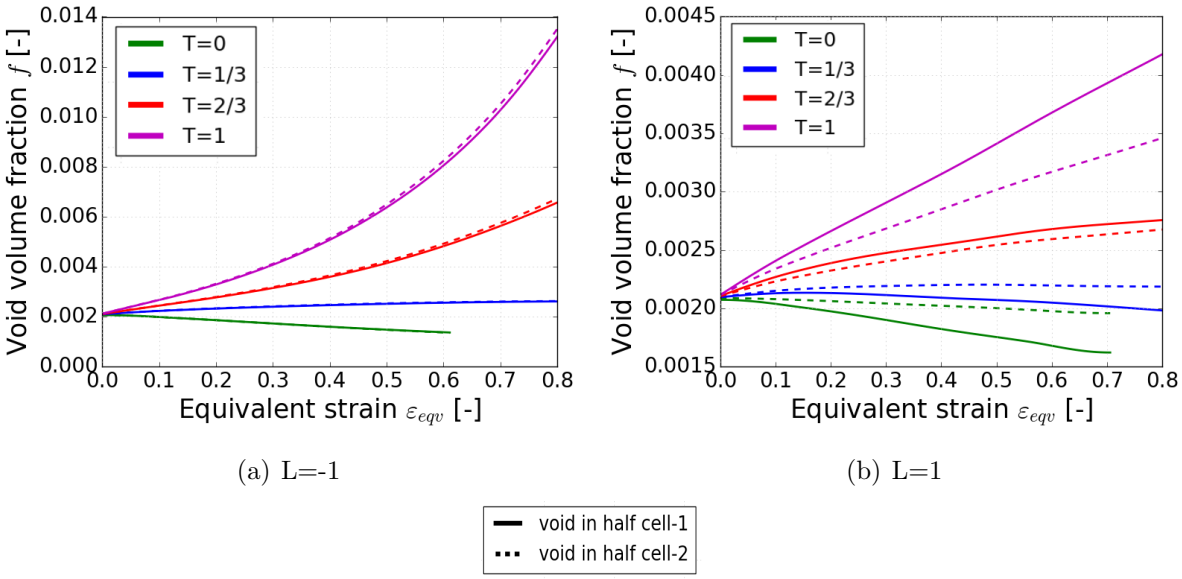

(a) L=-1 (b) L=1

Figure 5: Void volume evolution at different stress triaxialities and Lode parameters for the soft-soft bi-crystal. Matrix orientation of half cell 1 is O1 and half cell 2 is O2.

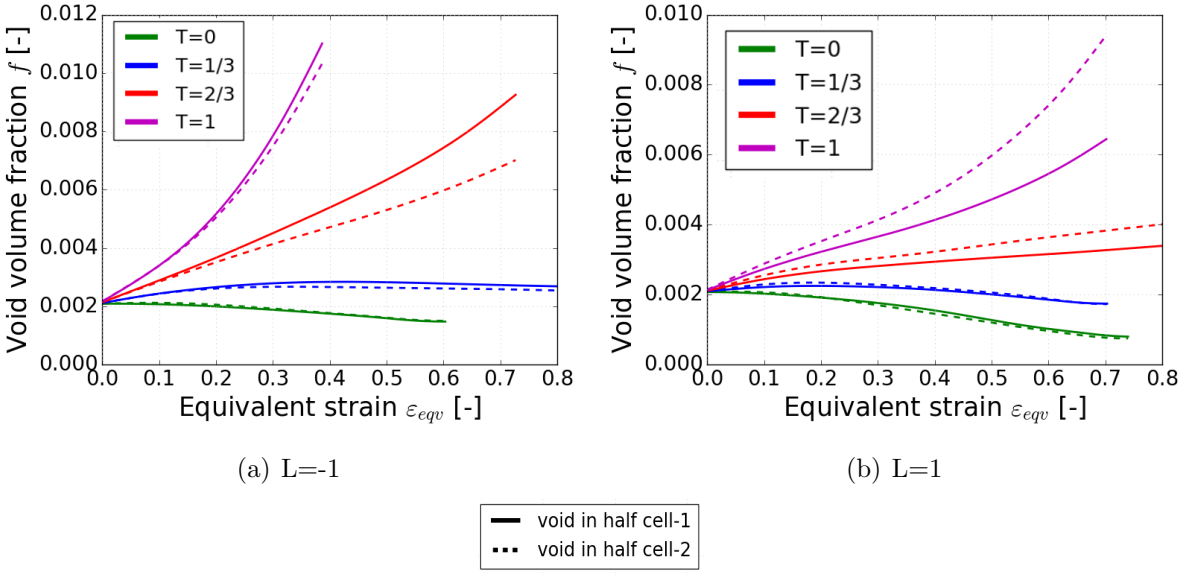

(a) L=-1 (b) L=1

Figure 6: Void volume evolution at different stress triaxialities and Lode parameters for the hard-hard bi-crystal. Matrix orientation of half cell 1 is O6 and half cell 2 is O4.

3.1.2. Void growth in a hard-hard bi-crystal.

For hard-hard bi-crystal RVE, half cell 1 has orientation O6 and half cell 2 has orientation O4. Similarly to previous comparison, void volume fraction evolution for different Lode parameters and triaxialities are plotted in figures 6.

For Lode parameter $L = -1$, void growth in half cell 1 is quite similar to void growth in half cell 2 for triaxiality $(T = 0, 1/3, 1)$. For triaxiality $T = 2/3$, we observe a different void growth behaviour in both half cells. Void in half cell 1 grows faster compared with void in half cell 2.

For Lode parameter $L = 1$, we can see distinction in void growth between half cell 1 and half cell 2 at moderate triaxialities ($T = 1, 2/3$), as void in half cell 2 grows faster than void in half cell 1. For the remaining triaxialities ($T = 0,\ 1/3$), there is no significant difference in the void growth in two half cells. Similarly to the soft-soft bicrystal, when calculating local triaxilities per each half cell it has been found that the local triaxilities in half cell 2 are higher than in half cell 1.

For $L = 0$, the difference in void growth in half cell 1 and half cell 2 is small. Void in half cell 1 grows faster than void in half cell 2. Plots are not presented for $L = 0$ for brevity. As in the case of soft-soft bi-crystal RVE, void growth rate is higher for Lode parameter $L = -1$, followed by $L = 0$ and finally by $L = 1$.

3.1.3. Void growth in a soft-hard bi-crystal.

For soft-hard bi-crystals, half cell 1 has orientation O1 (soft) and half cell 2 has orientation O4 (hard). Evolution of f versus ε_{eqv} for half cell 1 and half cell 2 for different values of T and L are given in figures 7. The way results are presented in figures 7 are different as in previous sections to clearly show the changes occurring at low triaxialities ($T = 0, 1/3$), as the amount of void growth is small compared to moderate triaxialities ($T = 1, 2/3$).

For $T = 0$, as we can see from figure 7(a), void volume fraction in both half cell 1 and half cell 2 decreases below the initial void volume fraction f_0. For half cell 1, void volume fraction increases slightly in the early stages of deformation, but starts dropping as deformation progresses, whereas void volume fraction f in half cell 2 drops faster than f in half cell 1 for all Lode parameters. Among the 3 Lode parameters considered, void volume fraction drops faster for $L = 1$, followed by $L = 0$ and least for $L = -1$ in both half cells.

Considering $T = 1/3$, as shown in figure 7(b), at $L = -1$, we can see that the volume of the void in half cell 1 increases, whereas in half cell 2, void volume fraction grows slightly up until $\varepsilon_{eqv} = 0.2$, but later on the void volume fraction decreases. For $L = 0$, void volume fraction in half cell 1 increases up to $\varepsilon_{eqv} = 0.3$, but for ε_{eqv} greater than 0.3 it starts decreasing, and during the final stages of deformation, void volume decreases below the initial value $f_0 = 0.0022$. For void in half cell 2 even though we see a slight increase in f until $\varepsilon_{eqv} = 0.2$, at higher ε_{eqv} void volume starts decreasing below f_0. For $L = 1$, void in half cell 1 and void in half cell 2 behaves similarly to the case of $L = 0$.

The behaviour of the void in half cell 1 is similar for both triaxialities $T = 2/3, 1$, as shown in figures 7(c) and 7(d) as we observe void growth. For void in half cell 2, we observe void growth for $T = 1$ and $L = -1, 0, 1$, but for $T = 2/3$ void growth is very small and gradually during the course of deformation, we observe void growth saturation (i.e. no change in f) for $L = 0$ and $L = -1$. For $T = 2/3, 1$, void in half cell 1 grows faster than void in half cell 2 irrespective of Lode parameters. In general void grows faster for $L = -1$, followed by $L = 0$ and $L = 1$.

The difference in the behaviour of the void in both half cells are significant. For moderate triaxialities, the effect of Lode parameter is more prominent for void in half cell 1 (soft) compared to void in half cell 2 (hard). For all triaxialities and Lode parameters values considered, f always grows faster (or shrinks slower) in half cell 1 (soft orientation) compared with half cell 2 (hard orientation).This general trend is following the formula (14) since the level of equivalent stress is much higher in the half cell 2 than in half cell 1, as seen in Figs. 3(a),3(b). Additionally, when calculating the average triaxialities per each half cell we have found almost two times higher values

in half cell 1 (soft) than in half cell 2 (hard). The values are included in Table B.5.

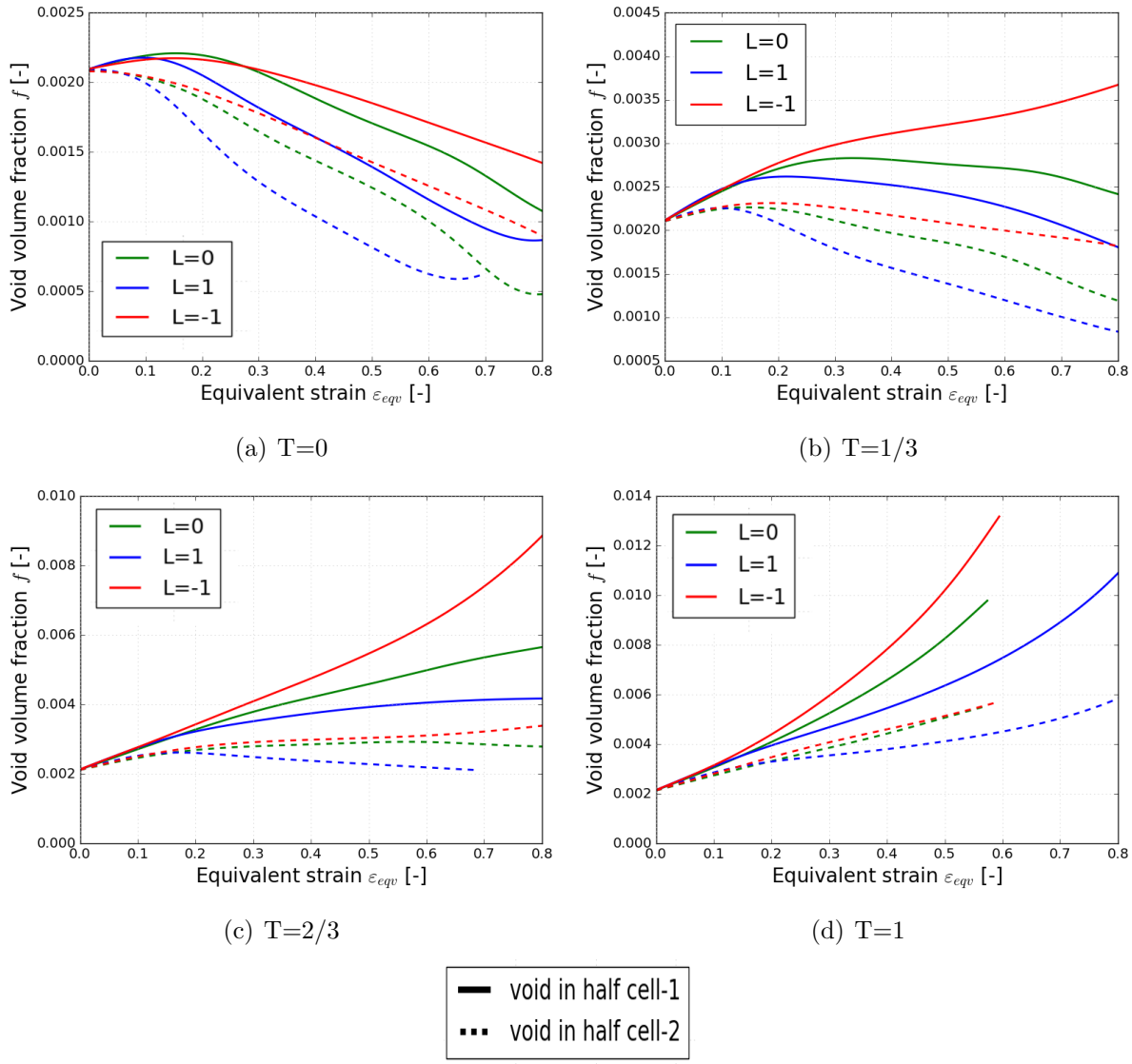

(a) T=0

(b) T=1/3

(c) T=2/3

(d) T=1

Figure 7: Void volume evolution at different stress triaxialities and Lode parameters for the soft-hard bi-crystal. Matrix orientation of half cell 1 is O1 and in half cell 2 is O4.

3.2. Deformed Void shape in a bi-crystal

In this section, we will present results on the influence of matrix orientation and stress state on void shapes and accumulated shear distribution $\gamma = \sum_\alpha \int_0^t |\dot{\gamma}^\alpha| \, dt$ on void shape evolution in different bi-crystal RVEs.

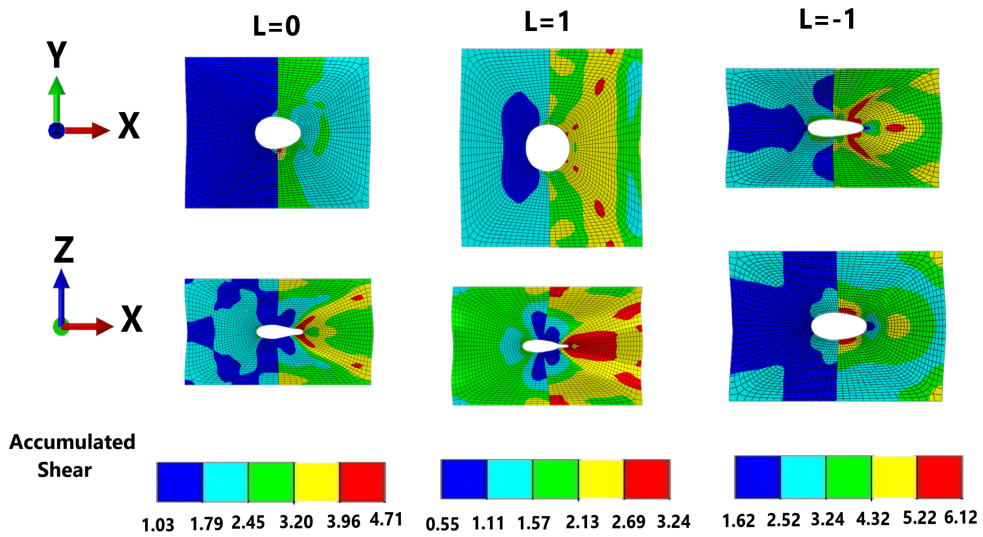

(a) T=0

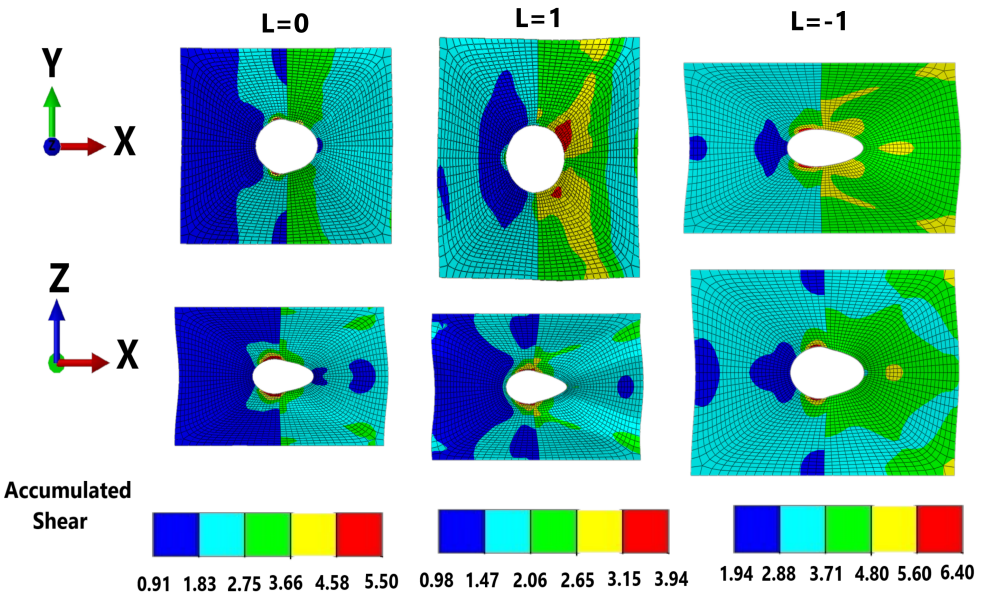

(b) T=1

Figure 8: Deformed void shape and distribution of accumulated shear γ for soft-hard bi-crystal at stress triaxiality $T = 0, 1$ and equivalent strain $\varepsilon_{eqv} = 0.45$ for $L = 0, 1, -1$.

3.2.1. Deformed void shape in a soft-hard bi-crystal

For soft-hard bi-crystal, at triaxiality $T = 0$, figure 8(a) shows the cross section of the deformed cell in two different planes (XY and XZ) at $\varepsilon_{eqv} = 0.45$ and the contours showing distribution of the accumulated shear γ for Lode parameters $L = 0, 1, -1$. As can be clearly seen from the plots, the distribution of γ and void shape in half cell 1 and half cell 2 are different for all the Lode parameters considered. For $L = 0$, the deformed cross-section of the cell along XY plane shows the void evolving into an ellipsoid on both half cells with the major axis of ellipsoid along

X axis (direction of the maximum applied stress). Looking at deformed cross section along XZ plane, we see the void in half cell 2 flattening into an elliptical crack like shape, with its major axis along X axis and the crack like surface arising from collapsing of void located away from the grain boundary, whereas void shape in half cell 1 is an oblate ellipsoid. The accumulated shear values are higher in half cell 2 compared with half cell 1 and the highest values of the accumulated shear is observed near the collapsed void surface in half cell 2, with a maximum value of 4.71.

From the deformed cell cross-section along XY axis, for $L = 1$, we see the void shape in both half cell 1 and half cell 2 to be circular at $\varepsilon_{eqv} = 0.45$. As in the case of $L = 0$, the void in half cell 2 collapses into a crack in XZ plane, with its tip along X axis and away from the grain boundary, whereas for void in half cell 1, the void evolves into an oblate ellipsoid. The value of the accumulated shear is higher in half cell 2 as compared to half cell 1 with a maximum value of 3.24.

For $L = -1$, the void shape in both half cell 1 and half cell 2 are very similar, and void evolves into an ellipsoid with the major axis along X. At $\varepsilon_{eqv} = 0.45$, we do not see void collapsing, but at higher strains void tend to collapse in both half cell 1 and half cell 2. Unlike $L = 0, 1$, for $L = -1$, void tends to collapse along Y axis and void radius evolves in the order $R_x > R_z > R_y$. Similar to the cases of $L = 0, 1$, the values of accumulated shear is higher in half cell 2. For the 3 Lode parameters analysed, the values of accumulated shear is higher for $L = -1$, followed by $L = 0$ and least by $L = 1$.

Similar analysis has been performed for $T = 1$ at Lode parameters $L = 0, 1, -1$ as shown in figure 8(b). As we discuss previously from figure 7(d), at $T = 1$ void growth is observed for all Lode parameters and the shape of the voids in both half cell 1 and half cell 2 are ellipsoid in all the cases, but there is a clear difference in the amount of growth within each half cell, as well as the void growth along each principal loading direction. Void radius is different along each direction and can be characterized as follows: for $\varepsilon_{eqv} = 0.45$ and for $L = 0$, void radius is of the order $R_x > R_y > R_z$ and for $L = 1$, order is $R_x = R_y > R_z$, finally $L = -1$ void radius is of order $R_x > R_z > R_y$. Accumulated shear values are higher in half cell 2 compared to half cell 1 and the value of the accumulated shear is higher for $L = -1$, followed by $L = 0$ and least in $L = 1$.

3.2.2. Deformed void shape in a hard-hard bi-crystal

In this section we will study void shape and accumulated shear distribution γ in the hard-hard bi-crystal, where the matrix orientation for half cell 1 is O6 and for half cell 2 is O4. Figure 9 shows the cross section of the deformed cell in XY and XZ planes, for $L = 0, 1, -1$ and $T = 0$ when $\varepsilon_{eqv} = 0.45$. For a hard-hard bi-crystal, we observe that the whole cell is deforming in such a way that it bends around the grain boundary. Such behaviour is understood when observing deformation of a respective bicrystal without a void for which in addition to axial deformation also shearing in opposite directions in two half cells is found. This shearing in XZ plane is also seen in Fig. 9. This is because of the anisotropic nature of the cell and the incompatibility between both half cells when hard-hard crystals comes in contact. This deformation behaviour of the cell has a huge influence on the way the void shape evolves. For $L = 0$, void shows elliptical shape with the major axis along X axis of the cell on both XY and XZ plane. Void shape is not symmetric along X axis of the cell and void radius along Z axis is higher in the upper part of the cell compared to the lower part along the grain boundary. The trend for void collapsing is clearly evident from the shape of the void. Void tends to collapse in half cell 2 faster than in half cell 1.

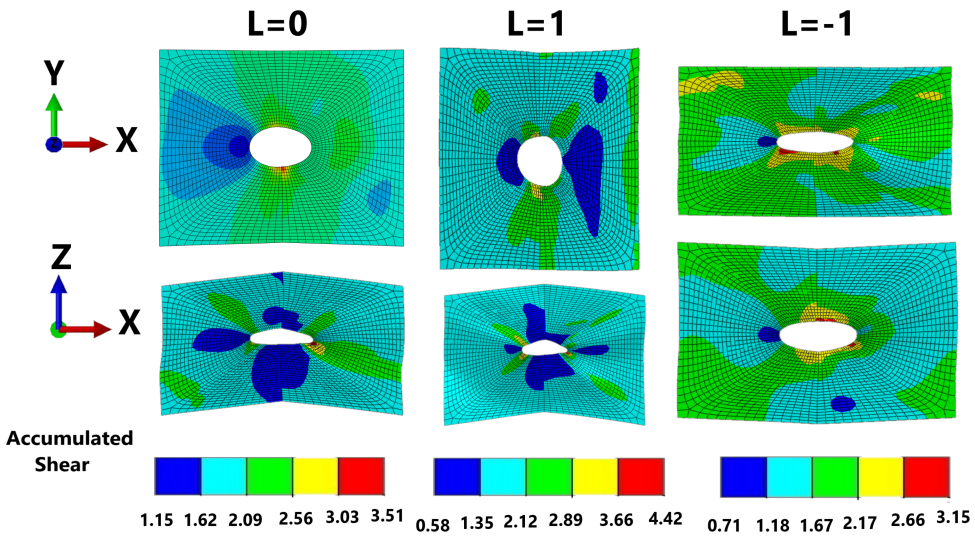

Figure 9: Deformed void shape and distribution of accumulated shear γ for a hard-hard bi-crystal at stress triaxiality $T = 0$ and equivalent strain $\varepsilon_{eqv} = 0.45$ for $L = 0, 1, -1$

Similarly, for $L = 1$ and along XY plane, we observe void shape being circular and along XZ plane void shape is irregular and it is unsymmetrical along X axis. Similar to the case of $L = 0$, void radius on the upper part of the cell in Z axis is higher than void radius in the lower part of the cell and void growth is observed along X and Y axis, whereas void collapse along Z axis. Finally for $L = -1$, void shape is elliptical in both half cells and in both XY and XZ planes. Void radius evolution is of the order $R_x > R_z > R_y$ and void tend to collapse along Y axis.

The location of the maximum value of accumulated shear is close to the void in half cell 2 for all 3 Lode parameters considered, and away from void we observe a homogeneous distribution of accumulated shear and similar values in both half cell 1 and half cell 2. At $\varepsilon_{eqv} = 0.45$ and $T = 0$, the maximum γ is found in $L = 1$ and has the value 4.42.

For $T = 1$ (results not shown here) and all Lode parameters considered, we observe elliptical void shapes in both XY and XZ planes. Void shape is similar in both half cells and the accumulated shear distribution is similar to the case $T = 0$.

3.3. *Effect of neighbouring grain orientation*

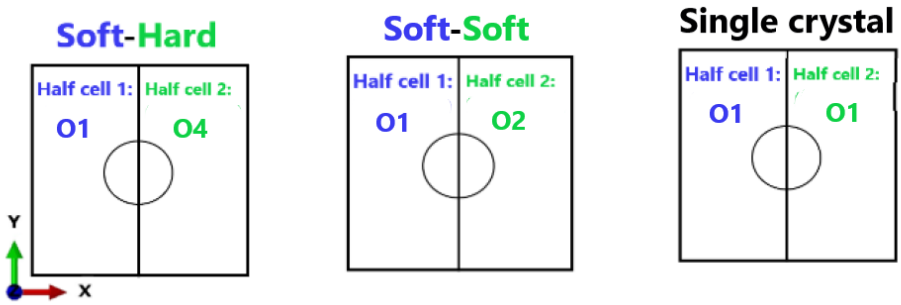

(a) soft-hard, soft-soft and single crystal with orientation O1

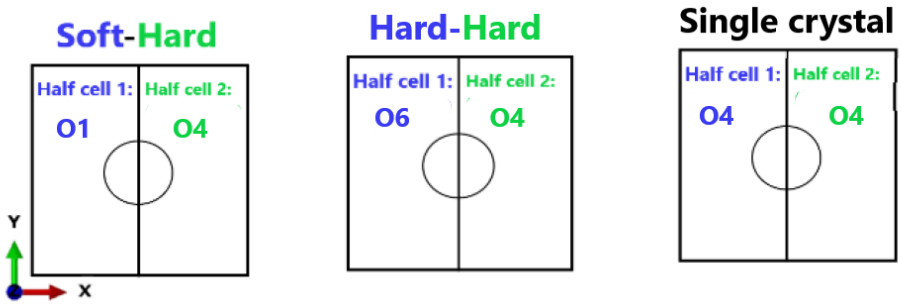

(b) soft-hard, hard-hard and single crystal with orientation 04

Figure 10: soft-hard, soft-soft, hard-hard bi-crystal and single crystal RVEs used for studying the effect of neighbouring grain orientation on the void behaviour. Blue colour represents orientations in half cell 1 and green colour represents orientation in half cell 2.

In this section, three different comparisons are made to study the effect of neighbouring grain orientation on void growth, 1. a matrix with hard orientation neighbour, 2. a matrix with soft orientation neighbour, and 3. neighbour grain with the same orientation (i.e., single crystal). For that end, first we will compare void evolution in half cell 1 of the soft-hard bi-crystal and soft-soft bi-crystal. As shown in figure 10(a), soft-hard bi-crystal and soft-soft bi-crystal has the same orientation for half cell 1 i.e., O1, but orientation of half cell 2 in soft-soft bi-crystal and soft-hard bi-crystal is different. Second, we will show results of void evolution in half cell 2 of hard-hard bi-crystal and soft-hard bi-crystal. For hard-hard bi-crystal and soft-hard bi-crystal orientation of half cell 2 is the same (i.e., O4 orientation), but orientation of half cell 1 in hard-hard bi-crystal and in soft-hard bi-crystal is different (see figure.10(b)).

Similarly, void behaviour is compared between half cell in a bi-crystal and half cell in a single crystal. The orientation of the single crystal is the same as half cell in the bi-crystal. For the case of the soft-hard bi-crystal, void in half cell 1 is compared with void in single crystal with the same orientation, i.e., O1, whereas for void in half cell 2 comparison is made with void in single crystal with the same orientation i.e., O4. By comparing the void behaviour in these cases, we can better understand the effect of neighbouring grain orientation on void behaviour and its morphology.

3.3.1. Void growth in soft-hard, soft-soft bi-crystals and single crystal

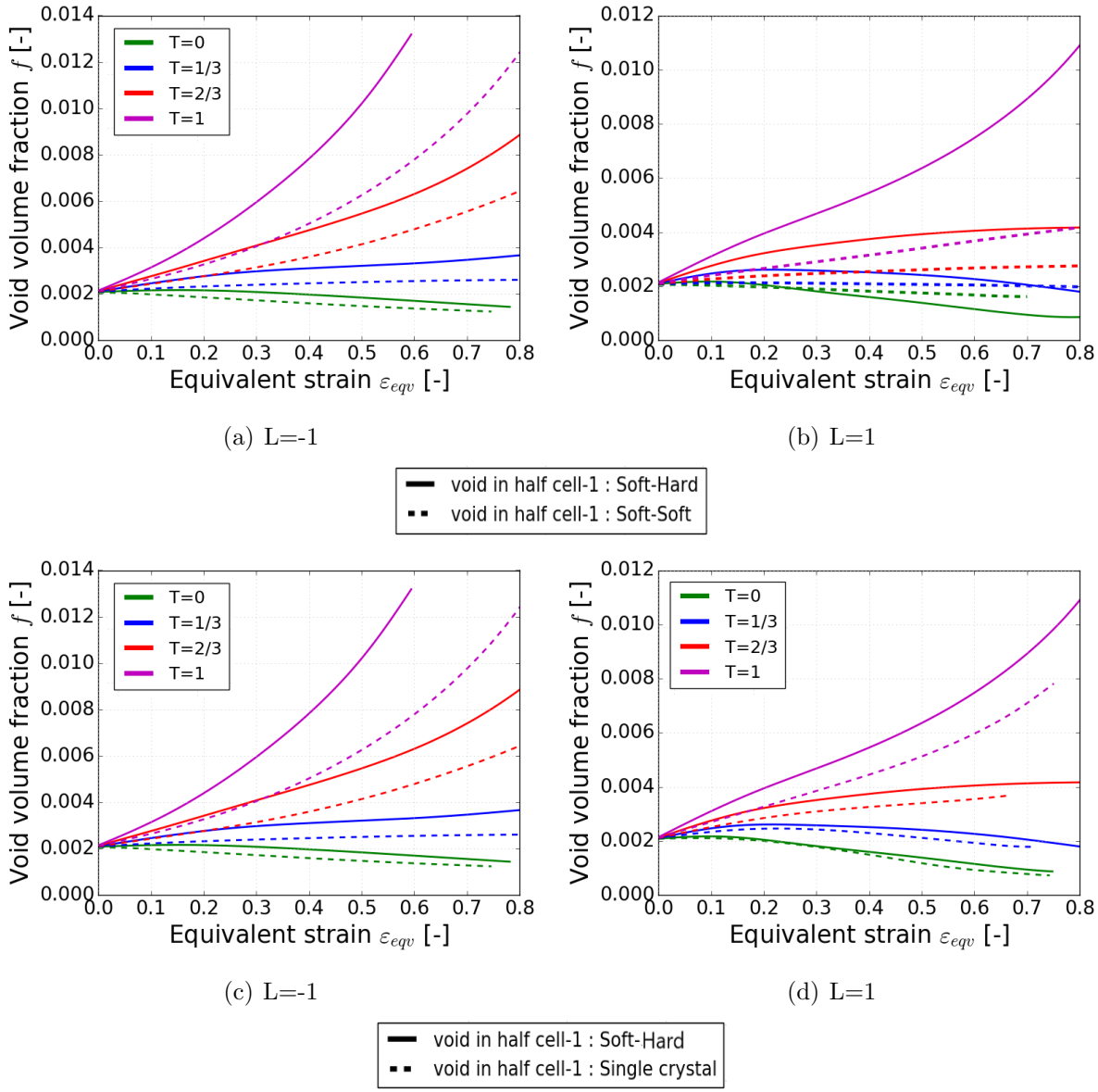

(a) L=-1 (b) L=1

(c) L=-1 (d) L=1

Figure 11: Comparison of void volume fraction-equivalent strain evolution for half cell 1 in soft-hard, soft-soft bi-crystals and in a single crystal with the same orientation as half cell 1 at different stress triaxialities $T = 0, 1/3, 2/3, 1$ and Lode parameters $L = 1,\ -1$.

In the case of soft-hard bi-crystal, soft-soft bi-crystal and single crystal, we will compare the effect of hard, soft and identical neighbouring matrix, respectively, on the void evolution in a soft matrix (half cell 1 is always O1 orientation). Figures 11 show void volume fraction-equivalent strain at different triaxialities and Lode parameters $L = -1, 1$. Figures 11(c) and 11(b) shows void volume evolution in half cell 1 for soft-soft and soft-hard bi-crystals. Figures 11(a) and 11(d) show void evolution in half cell 1 of soft-hard bi-crystal and of a single crystal. Single crystal calculations are performed for the full cell, but for comparison with bi-crystals, only half of the

cell is taken into account.

For Lode parameter $L = -1$, void in half cell 1 of soft-hard bi-crystal (continuous lines) grows faster than in soft-soft bi-crystal (dotted lines) for triaxialities $T = 1,\ 2/3$ as shown in figure 11(c). For triaxiality $T = 1/3$, void volume fraction in soft-hard bi-crystal increases slowly, whereas for soft-soft bi-crystal, void stops growing (i.e. void volume saturates after initial growth). For triaxiality $T = 0$, void volume fraction in both bi-crystals drop below f_0 from the beginning, and void in soft-soft bi-crystal drops faster than in soft-hard bi-crystal.

For $L = 1$ and $T = 1,\ 2/3$, as we can see from figure 11(b), void in half cell 1 of soft-hard bi-crystal grows faster than void of soft-soft bi-crystal and the difference in void volume evolution between both bi-crystals is smaller compared to $L = -1$. For $T = 1/3$, the amount of void growth in both bi-crystals is very less and void volume fraction in soft-hard bi-crystal is higher than in soft-soft bi-crystal. For $T = 0$, void volume in both bi-crystals drops below the initial volume f_0, dropping faster in soft-soft bi-crystal than in soft-hard bi-crystal.

Void evolution in half cell 1 for soft-hard bi-crystal and single crystal is presented in figures 11(a), 11(d). For $L = -1$ and for all triaxialities considered, void growth in half cell 1 in a soft-hard bi-crystal is higher than void growth in a single crystal. Interestingly, for $L = -1$, if we compare the void volume evolution of single crystal with half cell 1 of soft-soft bi-crystal shown previously in figure 11(c), we observe that the response of the void is the same for both cases at all triaxialities considered. This is explained by the same reason as almost the same response in two half cells seen in Fig. 5(a).

For $L = 1$ and $T = 1$ we observe that void growth in half cell 1 of soft-hard bi-crystal is much higher than void growth in a single crystal. For $T = 2/3,\ 1/3$, void growth in half cell 1 of soft-hard bi-crystal is higher than the single crystal case, but the difference in value of f is not as big as for $T = 1$. For $T = 0$, void volume fraction decreases below f_0 for both cases and void in half cell 1 of soft-hard bi-crystal drops slightly faster than void in single crystal. For $L = 1$ void behaviour in half cell 1 of soft-soft bi-crystal is closer to the void behaviour of the single crystal case.

The observed variation in the void growth for O1 orientation placed in these 3 different configurations for a given Lode parameter can be correlated with the hierarchy of an average triaxiality in the corresponding half cell 1 demonstrated in Table B5 and B6. Note that for a single crystal case its value is equal to the imposed triaxility.

3.3.2. Void growth in soft-hard, hard-hard bi-crystals and single crystal

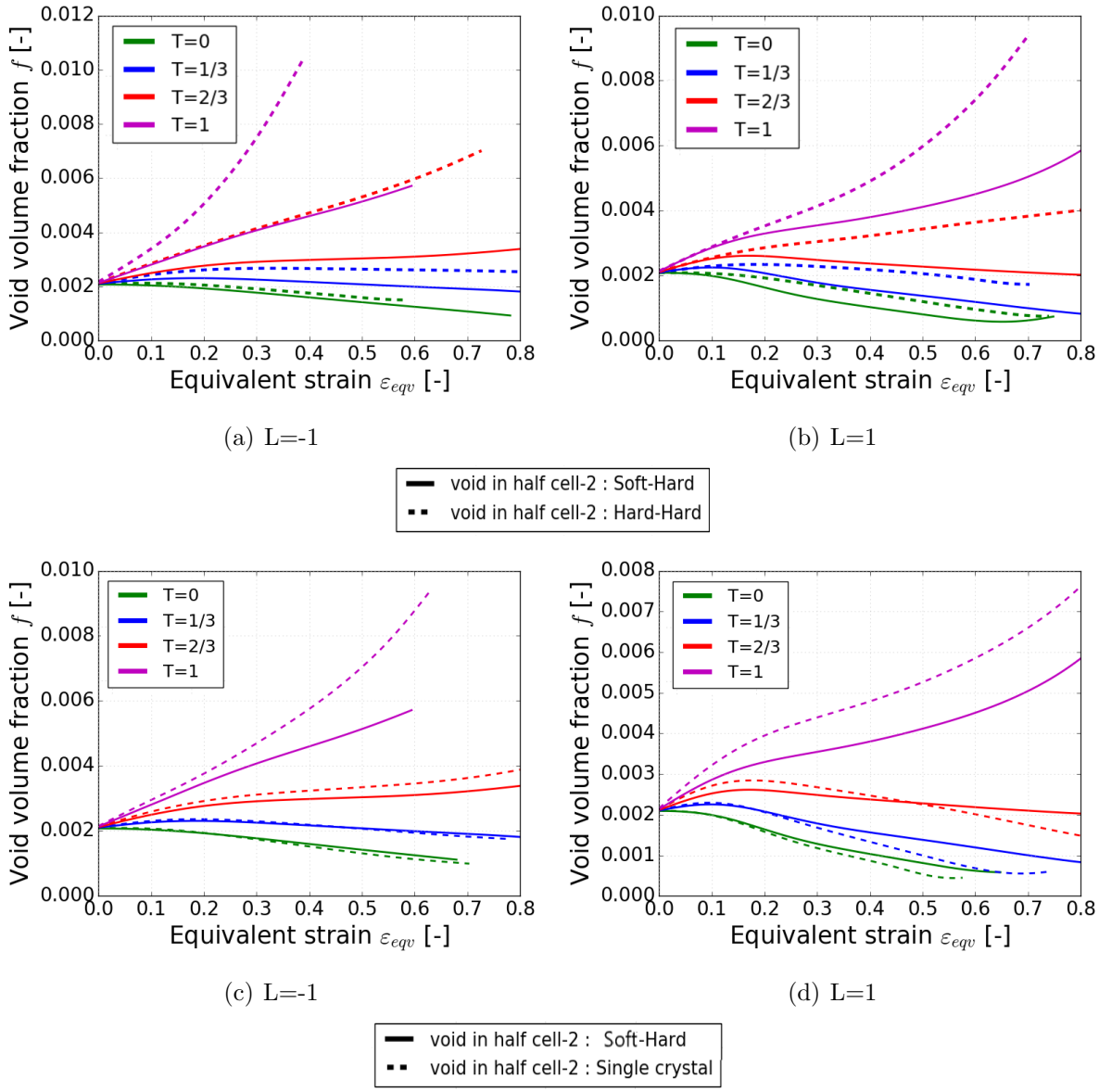

(a) L=-1 (b) L=1

(c) L=-1 (d) L=1

Figure 12: Comparison of void volume evolution-equivalent strain for half cell 2 in soft-hard, hard-hard bi-crystals and and single crystal with the same orientation as half cell 2 at different stress triaxialities $T = 0, 1, 1/3, 2/3$ and Lode parameters $L = 1, -1$.

In this section, the behaviour of the void in half cell 2 of a soft-hard bi-crystal is compared with the behaviour of the void in half cell 2 of hard-hard bi-crystal and single crystal with O4 orientation. The effect of a softer, harder and identical neighbouring matrix on the evolution of a void located in a hard matrix (half cell 2 is always O4 orientation) is compared and discussed.

Figures 12(a) and 12(b) show void volume fraction evolution with equivalent strain for voids of half cell 2 in a soft-hard (continuous lines) and in a hard-hard bi-crystal (dotted lines). For Lode parameter $L = -1$, void volume fraction in half cell 2 of a hard-hard bi-crystal grows faster

than half cell 2 in a soft-hard bi-crystal for triaxialities $T = 1, 2/3, 1/3$. The difference in void volume fraction evolution of both bi-crystals is less remarkable for $T = 1/3$ than for $T = 2/3,\ 1$. For T=0, void volume fraction for both bi-crystals drop below initial void volume fraction f_0 and void volume fraction of half cell 2 in soft-hard bi-crystal drops faster than half cell 2 in hard-hard bi-crystal. As we can see from the figure, void grows faster when the half cell has hard neighbour compared to soft neighbour.

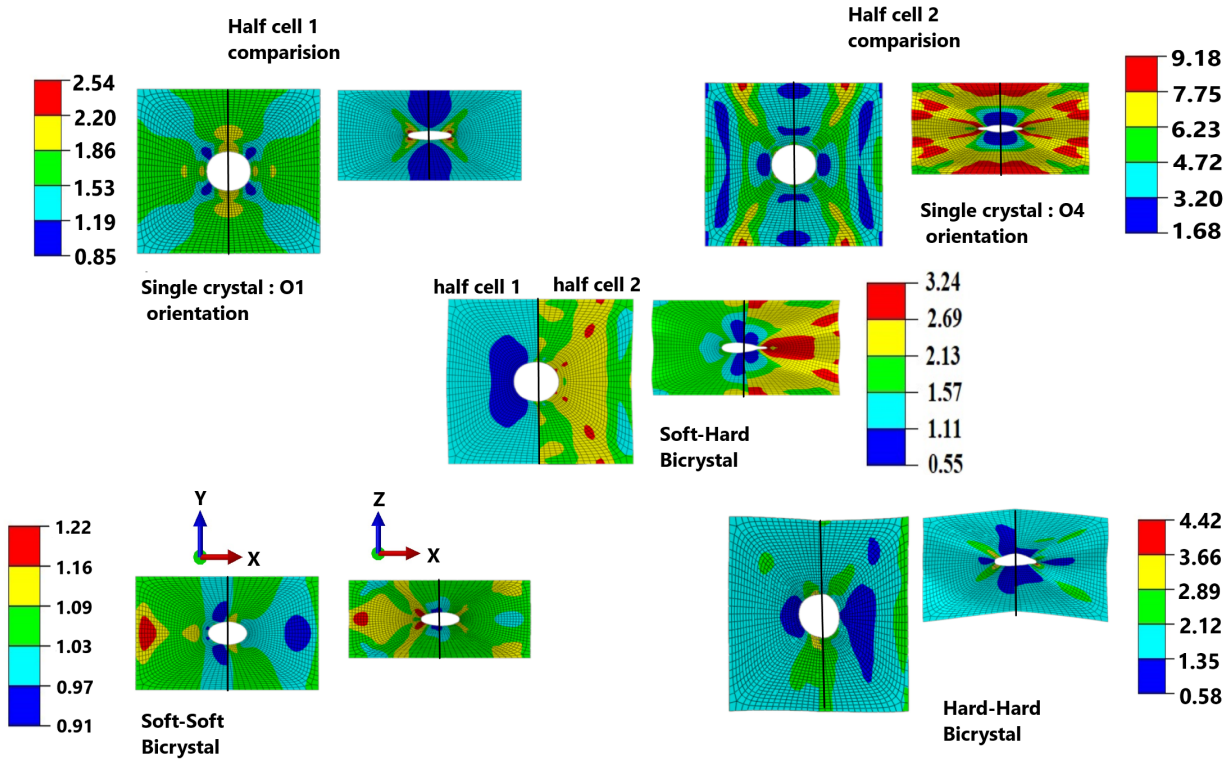

Figure 13: Cross section showing deformed void shape and accumulated shear γ for a (soft) single crystal, a (hard) single crystal, soft-hard bi-crystal, soft-soft bi-crystal and hard-hard bi-crystal for $T = 0$, $L = 1$ and $\varepsilon_{eqv} = 0.45$. The soft orientation in half cell 1 is always O1 and the hard orientation in half cell 2 is always O4 for configurations containing soft or hard component, respectively (see figure 10(a) and 10(b)).

Figure 12(b) shows void volume fraction evolution for Lode parameter $L = 1$. For $T = 1$, void volume fraction in both bi-crystals initially increases at the same rate, but at $\varepsilon_{eqv} > 0.15$ void volume in a hard-hard bi-crystal increases faster than in a soft-hard bi-crystal. For $T = 2/3$, we observe contrasting void behaviour in both bi-crystals: as f of a hard-hard bi-crystal gradually increases at constant rate, f of a soft-hard bi-crystal start decreasing below initial void volume fraction f_0. For $T = 1/3$ and $T = 0$, void volume fraction decreases in both bi-crystals below initial void volume fraction f_0, dropping faster in half cell 2 of a soft-hard bi-crystal than in a hard-hard bi-crystal.

Similarly, figures 12(c) and 12(d) show comparisons of half cell 2 void evolution for soft-hard bi-crystal (continuous lines) and for a single crystal with the same orientation as half cell 2 (dotted lines). Single crystal calculations are performed considering the full cell, but for comparison with

bi-crystals, only the behaviour of half cell is considered. For $L = -1$ and comparing soft-hard bi-crystal with a (hard) single crystal, we observe that, at $T = 1,\ 2/3$, void growth in the single crystal is higher than in the soft-hard bi-crystal. At $T = 1/3,\ 0$, void evolution f in the soft-hard bi-crystal is very similar to the single crystal case. For $L = 1$ and at $T = 1$, void growth in the single crystal is higher than in the soft-hard bi-crystal. For $T = 2/3$, we observe void growing in different way compared to other cases, as void volume fraction in both soft-hard bi-crystal and single crystal increases initially, but starts decreasing during final stages of deformation and void in single crystal drops faster than in soft-hard bi-crystal. For $T = 1/3, 0$ void volume decreases below initial void volume fraction for both cases and void volume fraction in single crystal drops faster than void in soft-hard bi-crystal.

Overall, for $L = -1\ , 1$ and at $T = 1$, void growth is higher in a hard-hard bi-crystal, followed by a (hard) single crystal and finally by a soft-hard bi-crystal. For $T = 1$ and $L = -1$, void evolution growing faster for orientation O4 than orientation O1 were also found by Ling et al. (2016) for a voided single crystal. At $T = 2/3$, f is higher in a hard-hard bi-crystal and the void behaviour of a soft-hard and a (hard) single crystal has similar trend. At $T = 1/3, 0$, void volume fraction decreases faster in a single crystal, followed by a soft-hard bi-crystal and finally by a hard-hard bi-crystal. The tendency for void collapse is higher in the single crystal case. For all triaxialities tested, the behaviour of the hard-hard bi-crystal is in general closer to the response of the single crystal case.

The calculated average triaxialities per each half cell included in Table B4 and B5 conform with the exposed tendencies. An additional role in shaping the void evolution is played by the specific deformation of a unit cell in the case of the hard-hard bi-crystal as demonstrated in the next section.

3.4. Effect of neighbouring grain orientation on the deformed void shape.

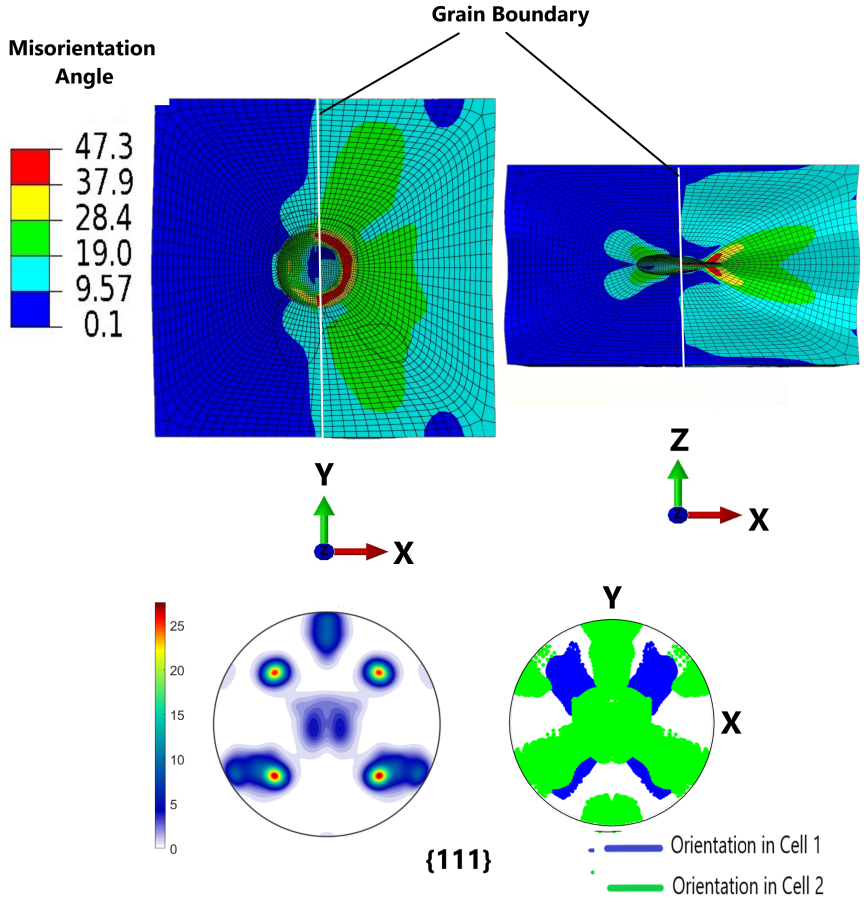

Figure 14: Distribution of misorientation angle with respect to the initial orientation for soft-hard bi-crystal for $T = 0$, $L = 1$ and equivalent strain 0.45, Pole figures 111 at the bottom present the spread of the current crystal orientations for each Gauss point in the cell (pole figure on the left is a density plot, pole figure on the right – discrete point plot.

It is clearly evident from the results presented in the previous section that void growth is affected by neighbouring grain orientation and, depending on the Lode parameter and triaxiality values, the behaviour of the void is either closer to a single crystal or its respective bi-crystal counterpart. In this section, the effect of neighbouring grain orientation on the void shape is presented and discussed. As in the previous section, the cases that are going to be compared are:

1. Void in half cell 1 in a soft-hard bi-crystal, void in half cell 1 in a soft-soft bi-crystal and in a single crystal with the same orientation as half cell 1 (O1).
2. Void in half cell 2 in a soft-hard bi-crystal, void in half cell 2 in a hard-hard bi-crystal and in a single crystal with the same orientation as half cell 2 (O4).

As noted by Srivastava and Needleman (2013, 2015a), changes in void shape in a initially spherical void are more significant at low triaxialities than at moderate or high triaxiality values. We now focus on studying the influence of neighbouring grain orientation on the deformed void

shape. We choose to present only one case here, i.e., triaxiality value $T = 0$ and $L = 1$ as a representative example. Deformed void shapes are compared in different RVEs at $\varepsilon_{eq} = 0.45$.

Fig. 13 shows the deformed void shape in single crystals with O1 and O4 orientation respectively, soft-soft, soft-hard and hard-hard bi-crystals. By comparing deformed void shape in half cell 1(left-half) in a soft-hard bi-crystal and in a single crystal with O1 orientation, we observe that void in half cell 1 is ellipsoidal in both RVEs at both XY and XZ planes, with void radius in order $R_x \approx R_y > R_z$. In the soft-soft bi-crystal case, we observe that void within half cell 1 is also ellipsoidal but the order of void radius is $R_x > R_y > R_z$. In a soft-hard bi-crystal void shape in half cell 2 (right-half) is quite similar to the void shape in a single crystal with O4 orientation in both XY and XZ planes. As we see from figure 13 for the aforementioned RVEs, void tends to collapse into a "crack like" shape along X direction, and void radius for both RVEs are in order $R_x \approx R_y > R_z$. For a hard-hard bi-crystal, void evolves into irregular shape before collapsing along XZ plane, but void collapse occurs at rate slower than for single crystal. By comparing accumulated shear in half cell 1 among soft-hard, soft-soft and single crystal RVE, the maximum value of accumulated shear is observed in single crystal with O1 orientation (soft orientation) in the vicinity of the void in XZ plane. Similarly comparing accumulated shear in half cell 2 among soft-hard, hard-hard and single crystal RVE, the maximum value of γ is obtained in single crystal with O4 orientation (hard orientation) in XZ plane. Overall, for $T = 0$, $L = 1$ and at $\varepsilon_{eq} = 0.45$, γ values are higher in (hard) single crystal, followed by hard-hard bi-crystal, soft-hard bi-crystal, (soft) single crystal and finally soft-soft bi-crystal.

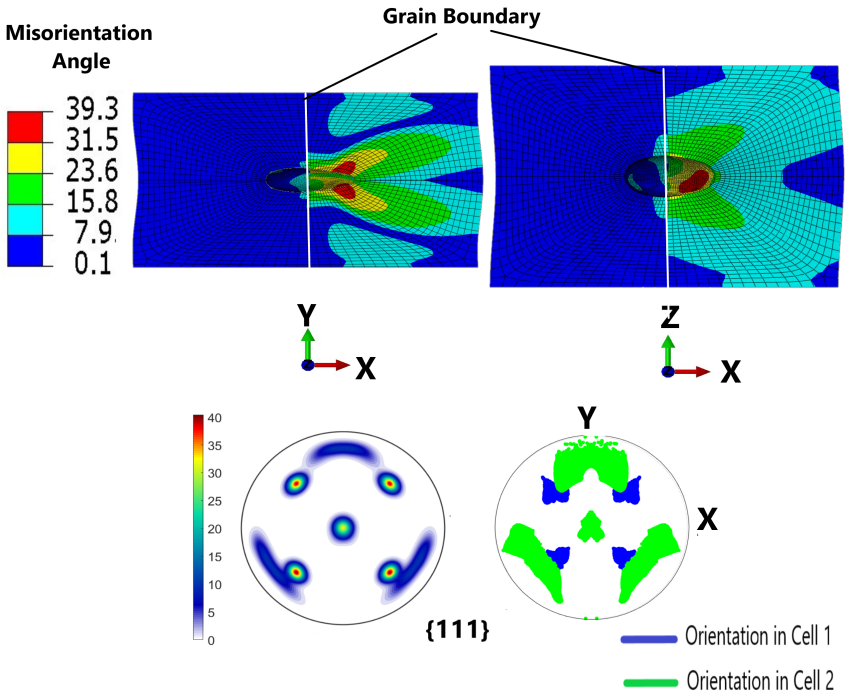

Figure 15: Distribution of misorientation angle with respect to the initial orientation for soft-hard bi-crystal for $T = 0$, $L = -1$ and equivalent strain 0.45, Pole figures (111) at the bottom present the spread of the current crystal orientations for each Gauss point in the cell (pole figure on the left is a density plot, pole figure on the right-discrete point plot.)

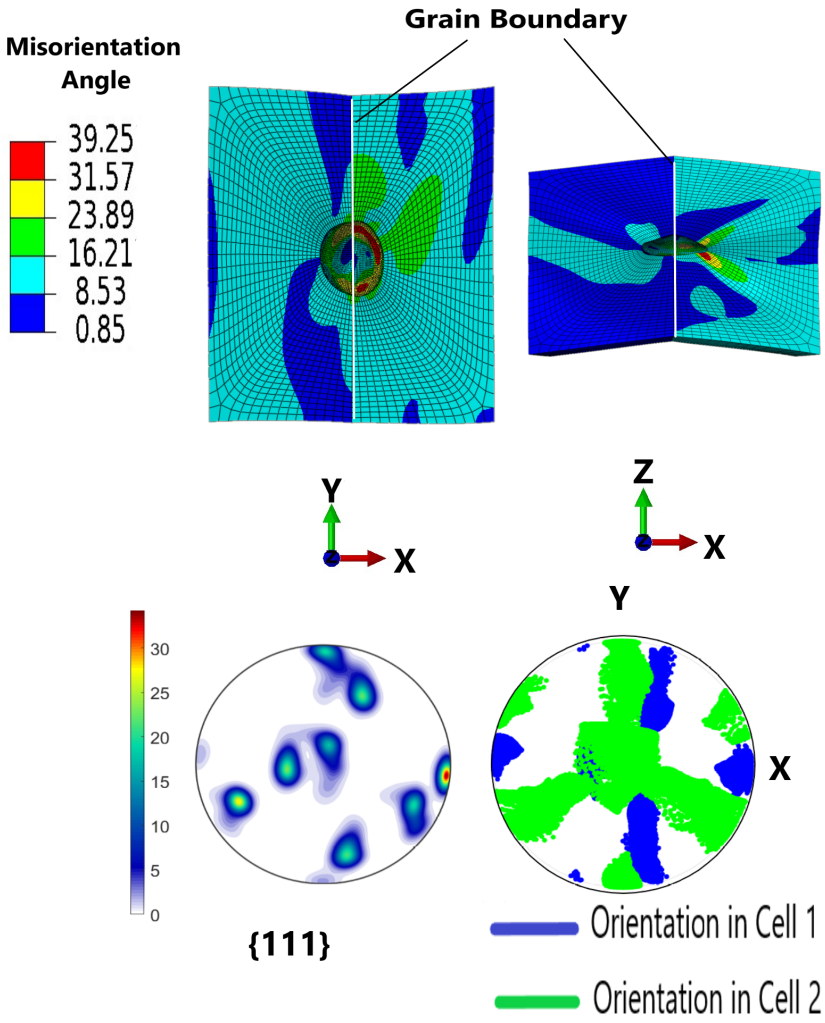

Figure 16: Distribution of misorientation angle with respect to the initial orientation for hard-hard bi-crystal for $T = 0$, $L = 1$ and equivalent strain 0.45, Pole figures 111 at the bottom present the spread of the current crystal orientations for each Gauss point in the cell (pole figure on the left is a density plot, pole figure on the right-discrete point plot.)

Figure 14, presents the influence of void on the heterogeneity of lattice rotation in the soft-hard bi-crystal, at $T = 0$ and $L = 1$. Let us stress that initially all elements within each half cell have the same orientation. While for a bi-crystal without a void, lattice rotates uniformly within each half cell (results are confirmed by calculations, but not presented here for brevity), strong variation is observed when the voids are present at the grain boundary. What is not obvious at first is that heterogeneity is more pronounced within hard half cell as initially homogeneous orientation in half cell is fragmented into two distinct orientations after deformation, as visible in the left pole figure. This is probably caused by the fact that different set of slip systems are operating in the top and bottom part of the half cell and the lattice is rotating in opposite directions in these two parts. Note that the largest misorientation angle ($> 45^o$) is observed close to the void boundary, where the void is distorted most. Figure 15 presents analogical results for the same bi-crystal but for $L = -1$ and $T = 0$. Here, also the larger misorientation angles are found in the hard

half cell. Note that in both cases observed, differences in misorientation angles between elements belonging to the hard half cell are often higher than 15^o, which suggests, appearance of new high angle boundaries and possibility of grain refinement. Smaller differences in misorientation angles in two half cells are observed for hard-hard bi-crystal in figure 16. Nevertheless, also in this case the presence of void leads to the non-uniform lattice rotation leading to an increase of a lattice curvature.

4. Summary and Conclusions

Three-dimensional finite element cell calculations are carried out with the aim of analysing the response of voids at the grain boundary of a bi-crystal RVE. The effect of crystal orientation on porosity evolution are studied for three different cases: soft-hard, soft-soft and hard-hard RVEs subjected to different loading conditions. Unit cells consisting of cubic cells divided in two halves with a spherical void at the grain boundary with total void volume fraction in the cell $f_0 = 0.0044$ and volume of void in each half cell $f_0 = 0.0022$ are analysed. The responses of bi-crystal RVEs are studied for four stress triaxiality values: $T = 0, 1/3, 2/3, 1$, three Lode parameters $L = -1, 0, 1$ with a strictly specified orientation of loading directions with respect to the initial bi-crystal orientation, and a dimensionless equivalent strain rate $\dot{\varepsilon}_{eqv}/\dot{\gamma}_0$ in the range (100 – 150). In order to select soft and hard orientations first calculations have been performed for the case of single crystal without voids. For a given Lode parameter, the orientation with higher values of equivalent stress are considered as hard orientations and orientations with lower values of equivalent stress are considered as soft orientations.

The evolution of void volume fraction strongly depends on the overall stress triaxiality and more specifically on the triaxiality for the stress averaged over each half cell for all bi-crystal RVEs considered. When the level of strain increases the Lode value of macroscopic loading importantly modifies this dependencies. Moreover the Lode value has a prominent effect on the evolving shape of void, which especially seen at low triaxialities. Even though all bi-crystal RVEs considered have high angle grain boundaries, significant difference in void growth between the two half cells occurs specially for soft-hard bi-crystal case. The different behaviour of the void evolution in each half cell can be attributed to the difference in the strength (soft-hard) between the two initial orientations (O1 and O4) and the incompatibility between the two half cells. In the soft-hard bi-crystal case, at high triaxialities, void grows faster in softer crystal compared to harder crystal counterpart, whereas at low triaxialities, void tends to collapse faster in harder half cell compared to neighbouring softer crystal. Void growth is higher for higher triaxialities and void growth is faster for $L = -1$, followed by $L = 0$ and $L = 1$.

Void shape evolution in bi-crystals depends on triaxiality, Lode parameter and initial orientation of each grain. At high triaxialities, void tends to evolve into spherical/ ellipsoidal shapes irrespective of Lode parameter and grain orientation. At low triaxialities, void shape is greatly affected by the initial bi-crystal orientation with respect to the assumed loading conditions specified by the Lode parameter as the void tend to evolve into ellipsoidal shapes for soft half cells, and into crack like shapes for hard half cells. Void shape in half cell 2 of soft-hard bi-crystal looks more similar to hard (O4) single crystal, rather than half cell 2 of hard-hard bi-crystal. Void shape in half cell 1 of soft-hard bi-crystal, half cell 1 of soft-soft bi-crystal and soft single crystal looks similar.

If the volume and morphology of voids with the same matrix orientation, but different neighbouring cell orientation are compared we observe that void tend to behave like the single crystal case (same orientation as bi-crystal half cell) if the difference in strength between two half's of the bi-crystal is small, i.e., in the cases soft-soft and hard-hard. When the difference in strength between the two half cells is higher (i.e., soft-hard) void behaviour tend to move away from the respective single crystal behaviour.

At high triaxialities, the profound effect the orientation of the neighbouring grain has on the evolution of the void volume becomes even more important than the orientation of the grain itself. Irrespective of Lode value, for void in half cell 1 of soft-soft, soft-hard bi-crystals and soft (O1) single crystal, void growth is faster in the soft grain when the neighbouring grain has hard orientation. For void in half cell 2 of soft-hard, hard-hard bi-crystal and hard (O4) single crystal, void grows faster in the hard grain if the counterpart has hard orientation.

Slip system activity also depends on triaxiality, Lode parameter and initial crystal orientation and far away from the void becomes similar to a fully dense crystal under the same imposed loading conditions. Depending on crystal orientation we have different Schmid factors, which in turn leads to different slip activity. Higher the value of stress triaxiality, higher will be the amount of slip activity, and hence higher plastic deformation in the matrix around the void, leading to higher void growth. For a soft-hard bi-crystal, at high triaxiality, the maximum value of accumulated shear occurs around the void in the softer part, and away from the void, slip activity in the harder part is higher. At low triaxiality, slip system activity is significantly higher in the harder part and the maximum value of accumulated shear is observed around the void also in the harder part, irrespective of Lode value. Moreover, in soft-hard bi-crystal the heterogeneity of slip activity, especially within the harder crystal increases leading to a non-uniform lattice rotation and consequently grain fragmentation. Slip activities dependence on Lode parameter is clearly evident from our studies. Slip activity is higher for $L = -1$, followed by $L = 0$ and least for $L = 1$, irrespective of triaxiality value. For hard-hard and soft-soft bi-crystals, slip activity away from the void is similar in both half cells and around the void maximum slip activity occurs.

The crystal plasticity model used in the present study is standard. Observed dependencies can be modified when enhanced strain gradient formulations Wulfinghoff et al. (2013); Stupkiewicz and Petryk (2016); Ling et al. (2018), which introduce size effects, are applied. For example, as recently demonstrated by Ling et al. (2018) using the reduced micromorphic finite strain crystal plasticity model, the void growth is slow down and the void coalescence delayed when the void size is small as compared to the intrinsic length scale of the material. It happens due to the modification of accumulated shear field close to the void. Similarly, the strain gradient formulation may help to account for the grain boundary effect on the resistance to plastic flow, as demonstrated by Wulfinghoff et al. (2013). This may affect the results obtained in the context of bicrystal. Therefore, in the future more advanced crystal plasticity formulations can be considered for the analysis of the grain boundary effect on the void growth.

Furthermore, to complement numerical results presented in this work and in order to extract definite conclusions, more numerical simulations should be developed and experimental campaigns focus on studying the evolution of intergranular voids in fcc bi-crystals should be designed and conducted in the future.

Acknowledgements

The research leading to these results has received funding from the European Union's Horizon 2020 Program (Excellent Science, Marie-Sklodowska-Curie Actions) under REA grant agreement 675602 (Project OUTCOME). We are thankful to Dr. Jose A. Rodríguez-Martínez of University Carlos III, Madrid, for numerous fruitful discussions.

Appendix A. Prescribed Boundary Conditions

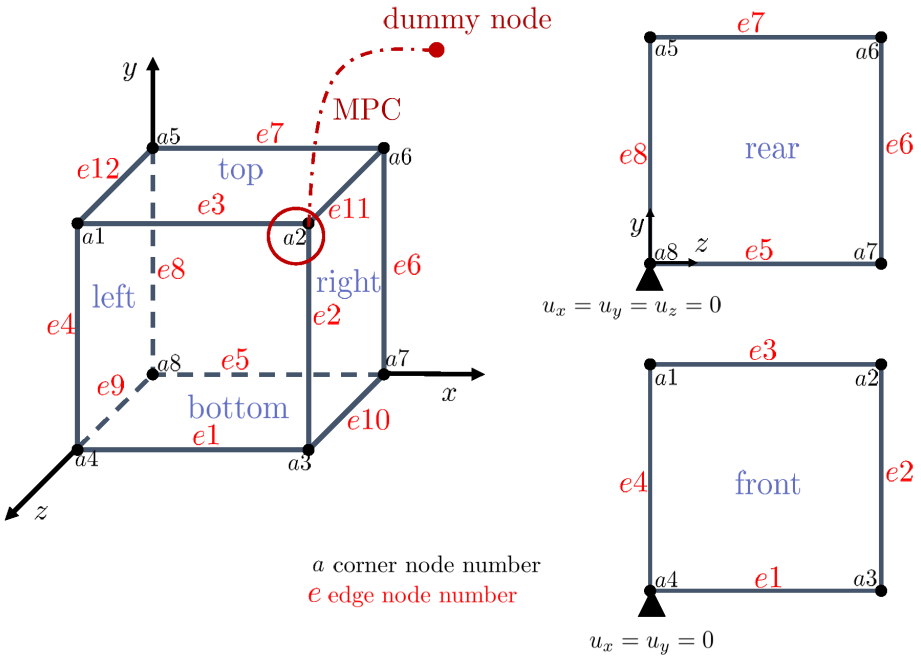

Figure A.17: Periodic boundary conditions applied to the 3D cell.

Boundary conditions applied for a representative volume element is described in detail in this section. In the undeformed cell, the edges of the cell are aligned along the coordinate axes (X,Y,Z), and the origin of the reference coordinate system corresponds to the node $a6$ (see Figure A16). The faces of the cell are initially straight and the nodes on the opposite faces are connected in order to obtain a periodic response from the cell. Apart from the periodic response, in the present work, constant values of stress triaxiality and Lode parameter are applied to the cell. The procedure to prescribe loading to keep constant values of macroscopic stress triaxiality and Lode parameter throughout the deformation history follows the work of Vadillo et al. (2016).

If the ratio of principal macroscopic true stress R and Q are defined in the form:

$$R = \frac{\sigma_2}{\sigma_1}; \qquad Q = \frac{\sigma_3}{\sigma_1}; \tag{A.1}$$

triaxiality T and Lode parameter L (Eq. (10)) can be written as:

$$T = \frac{\sqrt{2}(R+Q+1)}{3\sqrt{(1-R^2)+(1-Q^2)+(R^2-Q^2)}}; \quad L = \frac{2R-Q-1}{1-Q} \tag{A.2}$$

Since the macroscopic principal true stresses (σ_1, σ_2, σ_3) and the normal components of macroscopic strain rate in the basis of stress principal directions ($\dot{\varepsilon}_{11}$, $\dot{\varepsilon}_{22}$, $\dot{\varepsilon}_{33}$) are equal to the volume

average values in a cell (Hill (1967)), the total rate of deformation work in the whole cell $\dot{W}$ can be written as:

$$\dot{W} = V\sigma_1\dot{\varepsilon}_{11} + V\sigma_2\dot{\varepsilon}_{22} + V\sigma_3\dot{\varepsilon}_{33} \tag{A.3}$$

$\dot{W}$ can be also expressed in terms of the transformed rates of deformation and forces, as:

$$\dot{W} = V\sigma_{(I)}\dot{\varepsilon}_{(I)} + V\sigma_{(II)}\dot{\varepsilon}_{(II)} + V\sigma_{(III)}\dot{\varepsilon}_{(III)} \tag{A.4}$$

considering the transformation

$$\begin{pmatrix} \dot{\varepsilon}_{(I)} \\ \dot{\varepsilon}_{(II)} \\ \dot{\varepsilon}_{(III)} \end{pmatrix} = \mathbf{N} \begin{pmatrix} \dot{\varepsilon}_{11} \\ \dot{\varepsilon}_{22} \\ \dot{\varepsilon}_{33} \end{pmatrix}; \quad \begin{pmatrix} \sigma_{(I)} \\ \sigma_{(II)} \\ \sigma_{(III)} \end{pmatrix} = \mathbf{N} \begin{pmatrix} \sigma_1 \\ \sigma_2 \\ \sigma_3 \end{pmatrix}; \quad \text{with } \mathbf{N} = \begin{pmatrix} A_{11} & A_{12} & A_{13} \\ A_{21} & A_{22} & A_{23} \\ A_{31} & A_{32} & A_{33} \end{pmatrix}; \tag{A.5}$$

and:

$$\begin{aligned} A_{11} &= \frac{1}{\sqrt{1+R^2+Q^2}}; \quad A_{12} = \frac{R}{\sqrt{1+R^2+Q^2}}; \quad A_{13} = \frac{Q}{\sqrt{1+R^2+Q^2}} \\ A_{21} &= -\frac{R}{\sqrt{1+R^2}}; \qquad A_{22} = \frac{1}{\sqrt{1+R^2}}; \qquad A_{23} = 0. \\ A_{31} &= \frac{Q}{\sqrt{(1+R^2)\,(1+R^2+Q^2)}}; \quad A_{32} = \frac{RQ}{\sqrt{(1+R^2)\,(1+R^2+Q^2)}} \\ A_{33} &= -\frac{(1+R^2)}{\sqrt{(1+R^2)\,(1+R^2+Q^2)}} \end{aligned} \tag{A.6}$$

If in the transformed coordinate system, the three imposed incremental boundary conditions are prescribed as stress uniaxial:

$$\sigma_{(II)} = 0; \quad \sigma_{(III)} = 0; \quad \dot{\varepsilon}_{(I)} = \dot{\varepsilon}_{dummy} \tag{A.7}$$

the three prescribed boundary conditions in 1,2,3 directions, using $\mathbf{N}^{-1}$ relations are therefore:

$$R\sigma_1 - \sigma_2 = 0; \qquad Q\sigma_1 - \sigma_3 = 0; \qquad \dot{\varepsilon}_{11} + R\dot{\varepsilon}_{22} + Q\dot{\varepsilon}_{33} = \dot{\varepsilon}_{dummy}\sqrt{1+R^2+Q^2} \tag{A.8}$$

Values of $\dot{\varepsilon}_{11}$, $\dot{\varepsilon}_{22}$, $\dot{\varepsilon}_{33}$ and hence stress states (T and L) can be controlled in the cell by fixing properly values R and Q and prescribing incremental strain on an added dummy node. The multi-point constraints given in equations A.6, A.8 are implemented into ABAQUS/Standard (2019) via a user defined subroutine MPC.

Due to the anisotropy of the problem, and in order to determine a proper deformation behavior of the cell, periodic boundary conditions should be adopted in the external surfaces of the cell in all three directions. In this work, the general ideas of the implementation of periodic boundary conditions into a Finite Element solver given in (Segurado et al., 2002) is adopted. For the implementation of periodic boundary conditions, it is necessary to couple the displacements of opposite external nodes, on which an average macroscopic strain is allowed.

For simplicity and easy implementation, nodes on the surfaces of the cell are categorized into 3 different groups: corner nodes, edge nodes and surface nodes (see figure A16 for nomenclature details)

The node $a2$ is connected to the dummy node by the MPC subroutine, through which the average strains are applied to the system. This means that any deformation that is applied to the cell through the MPC has to be applied only connecting $a2$ to the added dummy node. In order to prescribe displacements in the outer surfaces which ensure periodicity:

$$u_i^{k+} - u_i^{k-} = E_{ij}\Delta x_j; \quad i,j = 1,2,3; \quad \Delta x_j = x_j^{k+} - x_j^{k-}; \quad \mathbf{t}^+ - \mathbf{t}^- = 0; \quad \mathbf{t} = \sigma.\mathbf{n} \tag{A.9}$$

being E_{ij} the macroscopic strain tensor and x_j the position vector, the following set of relations should be applied to the external nodes of the cell in order to avoid constraint linkages. These conditions are implemented in ABAQUS/Standard (2019) by the use of the command *Equation .

1. *For nodes on the faces of the cell:*

$$\begin{aligned}
u^{Top}(x,y,z) - u^{Bottom}(x,y,z) &= u^{a_5}(x,y,z) - u^{a_8}(x,y,z)\\
u^{Rear}(x,y,z) - u^{Front}(x,y,z) &= u^{a_8}(x,y,z) - u^{a_4}(x,y,z)\\
u^{Left}(x,y,z) - u^{Right}(x,y,z) &= u^{a_8}(x,y,z) - u^{a_7}(x,y,z)
\end{aligned}$$

2. *For nodes on the edges of the cell:*

$$\begin{aligned}
u^{e_7}(x,y,z) - u^{e_3}(x,y,z) &= u^{a_8}(x,y,z) - u^{a_4}(x,y,z)\\
u^{e_3}(x,y,z) - u^{e_1}(x,y,z) &= u^{a_5}(x,y,z) - u^{a_8}(x,y,z)\\
u^{e_1}(x,y,z) - u^{e_5}(x,y,z) &= u^{a_4}(x,y,z) - u^{a_8}(x,y,z)
\end{aligned}$$

$$\begin{aligned}
u^{e_{12}}(x,y,z) - u^{e_{11}}(x,y,z) &= u^{a_8}(x,y,z) - u^{a_7}(x,y,z)\\
u^{e_{11}}(x,y,z) - u^{e_{10}}(x,y,z) &= u^{a_5}(x,y,z) - u^{a_8}(x,y,z)\\
u^{e_{10}}(x,y,z) - u^{e_9}(x,y,z) &= u^{a_7}(x,y,z) - u^{a_8}(x,y,z)
\end{aligned}$$

$$\begin{aligned}
u^{e_8}(x,y,z) - u^{e_4}(x,y,z) &= u^{a_8}(x,y,z) - u^{a_4}(x,y,z)\\
u^{e_4}(x,y,z) - u^{e_2}(x,y,z) &= u^{a_8}(x,y,z) - u^{a_7}(x,y,z)\\
u^{e_2}(x,y,z) - u^{e_6}(x,y,z) &= u^{a_4}(x,y,z) - u^{a_8}(x,y,z)
\end{aligned}$$

3. *For nodes on the corner of the cell:*

$$\begin{aligned}
&u_x^{a_6} = u_x^{a_7}; \quad u_x^{a_3} = u_x^{a_2}; \quad u_x^{a_7} = u_x^{a_3}; \quad u_x^{a_1} = u_x^{a_4};\\
&u_y^{a_3} = u_y^{a_4}; \quad u_y^{a_1} = u_y^{a_2}; \quad u_y^{a_5} = u_y^{a_1}; \quad u_y^{a_6} = u_y^{a_5};\\
&u_z^{a_1} = u_z^{a_4}; \quad u_z^{a_4} = u_z^{a_2}; \quad u_z^{a_7} = u_z^{a_6}; \quad u_z^{a_3} = u_z^{a_2};\\
&u_{x,y,z}^{a_8} = 0; \quad u_{x,y}^{a_4} = 0;
\end{aligned}$$

Appendix B. Average triaxialities and Lode values in each half cell of the voided bi-crystal

Table B.4: Average local Triaxiality and Lode parameter for each half cell of hard-hard voided bi-crystal

Applied global T and L	Local T and L (half cell 1)	Local T and L (half cell 2)
$T = 0$, $L = -1$	$T = 0$, $L = -1$	$T = 0$, $L = -0.8$
$T = 0$, $L = 0$	$T = 0$, $L = 0$	$T = 0$, $L = 0$
$T = 0$, $L = 1$	$T = -0.2$, $L = 1$	$T = 0.23$, $L = 1$
$T = 0.33$, $L = -1$	$T = 0.33$, $L = -1$	$T = 0.33$, $L = -1$
$T = 0.33$, $L = 0$	$T = 0.33$, $L = 0$	$T = 0.3$, $L = 0$
$T = 0.33$, $L = 1$	$T = 0.22$, $L = 1$	$T = 0.4$, $L = 1$
$T = 0.66$, $L = -1$	$T = 0.66$, $L = -1$	$T = 0.66$, $L = -1$
$T = 0.66$, $L = 0$	$T = 0.66$, $L = 0$	$T = 0.66$, $L = 0$
$T = 0.66$, $L = 1$	$T = 0.53$, $L = 1$	$T = 0.72$, $L = 1$
$T = 1$, $L = -1$	$T = 1$, $L = -1$	$T = 1$, $L = -0.86$
$T = 1$, $L = 0$	$T = 1$, $L = 0.1$	$T = 1$, $L = -0.1$
$T = 1$, $L = 1$	$T = 1$, $L = 1$	$T = 1$, $L = 1$

Table B.5: Average local Triaxiality and Lode parameter for each half cell of soft-hard voided bi-crystal

Applied global T and L	Local T and L (half cell 1)	Local T and L (half cell 2)
$T = 0$, $L = -1$	$T = 0$, $L = -1$,	$T = 0$, $L = -0.8$
$T = 0$, $L = 0$	$T = 0$, $L = 0$	$T = 0$, $L = 0$
$T = 0$, $L = 1$	$T = 0$, $L = 1$	$T = 0$, $L = 1$
$T = 0.33$, $L = -1$	$T = 0.64$, $L = -1$	$T = 0.14$, $L = -1$
$T = 0.33$, $L = 0$	$T = 0.6$, $L = 0$	$T = 0.3$, $L = 0$
$T = 0.33$, $L = 1$	$T = 0.48$, $L = 1$	$T = 0.22$, $L = 1$
$T = 0.66$, $L = -1$	$T = 0.85$, $L = -1$,	$T = 0.5$, $L = -1$
$T = 0.66$, $L = 0$	$T = 1$, $L = 0$	$T = 0.4$, $L = 0$
$T = 0.66$, $L = 1$	$T = 0.86$, $L = 1$	$T = 0.51$, $L = 1$
$T = 1$, $L = -1$;	$T = 1.43$, $L = -1$,	$T = 0.65$, $L = -0.86$
$T = 1$, $L = 0$	$T = 1.61$, $L = 0.1$,	$T = 0.62$, $L = -0.1$
$T = 1$, $L = 1$	$T = 1.3$, $L = 1$	$T = 0.78$, $L = 1$

Table B.6: Average local Triaxiality and Lode parameter for each half cell of soft-soft voided bi-crystal

Applied global T and L	Local T and L (half cell 1)	Local T and L (half cell 2)
$T = 0$, $L = -1$	$T = 0$, $L = -1$	$T = 0$, $L = -0.8$
$T = 0$, $L = 0$	$T = 0$, $L = 0$	$T = 0$, $L = 0$
$T = 0$, $L = 1$	$T = -0.2$, $L = 1$	$T = 0.23$, $L = 1$
$T = 0.33$, $L = -1$	$T = 0.33$, $L = -1$	$T = 0.33$, $L = -1$
$T = 0.33$, $L = 0$	$T = 0.33$, $L = 0$	$T = 0.3$, $L = 0$
$T = 0.33$, $L = 1$	$T = 0.22$, $L = 1$	$T = 0.4$, $L = 1$
$T = 0.66$, $L = -1$	$T = 0.66$, $L = -1$	$T = 0.66$, $L = -1$
$T = 0.66$, $L = 0$	$T = 0.66$, $L = 0$	$T = 0.66$, $L = 0$
$T = 0.66$, $L = 1$	$T = 0.66$, $L = 1$	$T = 0.66$, $L = 1$
$T = 1$, $L = -1$	$T = 1$, $L = -1$	$T = 1$, $L = -0.86$
$T = 1$, $L = 0$	$T = 1$, $L = -0.11$	$T = 1$, $L = 0.11$
$T = 1$, $L = 1$	$T = 1$, $L = 1$	$T = 1$, $L = 1$

References

ABAQUS/Standard, 2019. Simulia, User's Manual. Dassault Systémes, Providence, USA. version 6.19 edition.

Asaro, R.J., Needleman, A., 1985. Textured development and strain hardening in rate dependent polycrystals. Acta metall. 33, 923–953.

Basu, S., Dogan, E., Kondori, B., Karaman, I., Benzerga, A., 2017. Towards designing anisotropy for ductility enhancement: A theory-driven investigation in mg-alloys. Acta Materialia 131, 349 – 362.

Benzerga, A.A., Besson, J., 2001. Plastic potentials for anisotropic porous solids. European Journal of Mechanics - A/Solids 20, 397 – 434.

Besson, J., 2010. Continuum models of ductile fracture: A review. International Journal of Damage Mechanics 19, 3–52.

Bringa, E.M., Traiviratana, S., Meyers, M.A., 2010. Void initiation in fcc metals: Effect of loading orientation and nanocrystalline effects. Acta Materialia 58, 4458 – 4477.

de Botton, G., Ponte Castañeda, P., 1995. Variational estimates for the creep behavior of polycrystals. Proc. R. Soc. London A448, 121–142.

Deshpande, N.U., Gokhale, A.M., Denzer, D.K., Liu, J., 1998. Relationship between fracture toughness, fracture path, and microstructure of 7050 aluminum alloy: Part I. Quantitative characterization. Metallurgical and Materials Transactions A 29, 1191–1201.

Dorward, R.C., Beerntsen, D., 1995. Grain structure and quench-rate effects on strength and toughness of AA7050 Al-Zn-Mg-Cu-Zr alloy plate. Metallurgical and Materials Transactions A 26, 2481–2484.

Fourmeau, M., Børvik, T., Benallal, A., Hopperstad, O., 2013. Anisotropic failure modes of high-strength aluminium alloy under various stress states. International Journal of Plasticity 48, 34 – 53.

Furnémont, F.L.Q., Rompaey, T.V., Delannay, F., Jacques, P., Pardoen, T., 2007. Multiscale mechanics of TRIP-assisted multiphase steels: II. Micromechanical modelling. Acta Materialia Volume 55, Issue 11, 3695–3705.

Gurson, A.L., 1977. Continuum Theory of Ductile Rupture by Void Nucleation and Growth: Part I—Yield Criteria and Flow Rules for Porous Ductile Media. Journal of Engineering Materials and Technology 99, 2–15.

Han, X., Besson, J., Forest, S., Tanguy, B., Bugat, S., 2013. A yield function for single crystals containing voids. International Journal of Solids and Structures 50, 2115 – 2131.

Hill, R., 1967. The essential structure of constitutive laws for metal composites and polycrystals. Journal of the Mechanics and Physics of Solids 15, 79–95.

Jeong, W., Lee, C.H., Moon, J., Jang, D., Lee, M.G., 2018. Grain scale representative volume element simulation to investigate the effect of crystal orientation on void growth in single and multi-crystals. Metals 8.

Kadkhodapour, J., Butz, A., Rad, S.Z., 2011a. Mechanisms of void formation during tensile testing in a commercial, dual-phase steel. Acta Materialia 59, 2575 – 2588.

Kadkhodapour, J., Butz, A., Ziaei-Rad, S., Schmauder, S., 2011b. A micro mechanical study on failure initiation of dual phase steels under tension using single crystal plasticity model. International Journal of Plasticity 27, 1103 – 1125.

Kalidindi, S.R., Bronkhorst, C.A., Anand, L., 1992. Crystallographic texture evolution in bulk deformation processing of fcc metals. J. Mech. Phys. Solids 40, 537–569.

Keralavarma, S., Benzerga, A., 2010. A constitutive model for plastically anisotropic solids with non-spherical voids. Journal of the Mechanics and Physics of Solids 58(6), 874–901.

Keralavarma, S., Reddi, D., Benzerga, A., 2020. Ductile failure as a constitutive instability in porous plastic solids. Journal of the Mechanics and Physics of Solids 139, 103917.

Lani, F., Furnémont, Q., Rompaey, T.V., Delannay, F., Jacques, P., Pardoen, T., 2007. Multiscale mechanics of trip-assisted multiphase steels: I. micromechanical modelling. Acta Materialia Volume 55, Issue 11, 3681–3693.

Ling, C., Besson, J., Forest, S., Tanguy, B., Latourte, F., Bosso, E., 2016. An elastoviscoplastic model for porous single crystals at finite strains and its assessment based on unit cell simulations. International Journal of Plasticity 84, 58–87.

Ling, C., Forest, S., Besson, J., Tanguy, B., Latourte, F., 2018. A reduced micromorphic single crystal plasticity model at finite deformations. application to strain localization and void growth in ductile metals. International Journal of Solids and Structures 134, 43–69.

Liu, W., Huang, H., Tang, J., 2010. FEM simulation of void coalescence in FCC crystals. Computational Materials Science 50, 411 – 418.

Liu, W., Zhang, X., Tang, J., 2009. Study on the growth behavior of voids located at the grain boundary. Mechanics of Materials 41, 799 – 809.

Liu, W., Zhang, X., Tang, J., Du, Y., 2007. Simulation of void growth and coalescence behavior with 3d crystal plasticity theory. Computational Materials Science 40, 130 – 139.

Mbiakop, A., Constantinescu, A., Danas, K., 2015. A model for porous single crystals with cylindrical voids of elliptical cross-section. International Journal of Solids and Structures 64-65, 100 – 119.

Meissonnier, F., Busso, E., O'Dowd, N., 2001. Finite element implementation of a generalised non-local rate-dependent crystallographic formulation for finite strains. International Journal of Plasticity 17, 601 – 640.

Morere, B., Ehrström, J.C., Gregson, P.J., Sinclair, I., 2000. Microstructural effects on fracture toughness in AA7010 plate. Metallurgical and Materials Transactions A 31, 2503–2515.

O'Regan, T.L., Quinn, D.F., Howe, M.A., McHugh, P.E., 1997. Void growth simulations in single crystals. Computational Mechanics 20, 115–121.

Papaefthymiou, S., Prahl, U., Bleck, W., van der Zwaag, S., Sietsma, J., 2006. Experimental observations on the correlation between microstructure and fracture of multiphase steels: Dedicated to professor eckard macherauch on the occasion of the 80th anniversary of his birth. Zeitschrift für Metallkunde 97, 1723–1731.

Paux, J., Morin, L., Brenner, R., Kondo, D., 2015. An approximate yield criterion for porous single crystals. European Journal of Mechanics - A/Solids 51, 1 – 10.

Perez-Bergquist, A., Cerreta, E., Trujillo, C., Cao, F., Gray, G., 2011. Orientation dependence of void formation and substructure deformation in a spalled copper bicrystal. Scripta Materialia 65, 1069 – 1072.

Potirniche, G., Hearndon, J., Horstemeyer, M., Ling, X., 2006. Lattice orientation effects on void growth and coalescence in fcc single crystals. International Journal of Plasticity 22, 921–942.

Segurado, J., Llorca, J., González, C., 2002. On the accuracy of mean-field approaches to simulate the plastic deformation of composites. Scripta Materialia 46, 525 – 529.

Selvarajou, B., Joshi, S.P., Benzerga, A.A., 2019. Void growth and coalescence in hexagonal close packed crystals. Journal of the Mechanics and Physics of Solids 125, 198 – 224.

Song, D., Castañeda, P.P., 2017. Macroscopic response of strongly anisotropic porous viscoplastic single crystals and applications to ice. Extreme Mechanics Letters 10, 41 – 49. Filling Gaps in Material Property Space: IUTAM Symposium.

Srivastava, A., Needleman, A., 2013. Void growth versus void collapse in a creeping single crystal. Journal of the Mechanics and Physics of Solids 61, 1169 – 1184.

Srivastava, A., Needleman, A., 2015a. Effect of crystal orientation on porosity evolution in a creeping single crystal. Mechanics of Materials 90, 10 – 29. Proceedings of the IUTAM Symposium on Micromechanics of Defects in Solids.

Srivastava, A., Needleman, A., 2015b. Effect of crystal orientation on porosity evolution in a creeping single crystal. Mechanics of Materials 90, 10 – 29. Proceedings of the IUTAM Symposium on Micromechanics of Defects in Solids.

Stupkiewicz, S., Petryk, H., 2016. A minimal gradient-enhancement of the classical continuum theory of crystal plasticity. part ii: Size effects. Archives of Mechanics 68, 487–513.

Tvergaard, V., Needleman, A., 1984. Analysis of the cup-cone fracture in a round tensile bar. Acta Metallurgica 32, 157 – 169.

Vadillo, G., Reboul, J., Fernández-Sáez, J., 2016. A modified gurson model to account for the influence of the Lode parameter at high triaxialities. European Journal of Mechanics A/Solids 56, 31–44.

Wulfinghoff, S., Bayerschen, E., Böhlke, T., 2013. A reduced micromorphic single crystal plasticity model at finite deformations. application to strain localization and void growth in ductile metals. International Journal of Plasticity 51, 33–46.

Yerra, S., Tekoğlu, C., Scheyvaerts, F., Delannay, L., Houtte, P.V., Pardoen, T., 2010. Void growth and coalescence in single crystals. International Journal of Solids and Structures 47, 1016 – 1029.